OXFORD

Journal of Petrology, 2025, **66**, egaf033
https://doi.org/10.1093/petrology/egaf033
ADVANCE ACCESS PUBLICATION DATE 16 APRIL 2025
Original Manuscript

Taking the Temperature of Ocean Islands: A Petrological Approach

WEI-RAN LI[1,2,*], OLIVER SHORTTLE[1,3], JOHN MACLENNAN[1], SIMON MATTHEWS[4], YISHEN ZHANG[5], OLIVIER NAMUR[6], CAROLINE R. SODERMAN[1] and DENNIS GEIST[7]

[1]Department of Earth Sciences, University of Cambridge, Downing Street, Cambridge CB2 3EQ, UK
[2]VRock Laboratory, Department of Earth Sciences, The University of Hong Kong, Pokfulam Road, Hong Kong 000000, China
[3]Institute of Astronomy, University of Cambridge, Madingley Road, Cambridge CB3 0HA, UK
[4]Institute of Earth Sciences, University of Iceland, Sturlugata 7, 102 Reykjavík, Iceland
[5]Department of Earth, Environmental and Planetary Sciences, Rice University, 6100 Main Street, Houston, TX 77005, USA
[6]Department of Earth and Environmental Sciences, KU Leuven, Celestijnenlaan 200E, Leuven 3001, Belgium
[7]Department of Geology, Colgate University, 13 Oak Drive, Hamilton, NY 13346, USA

[*]Corresponding author. Fax: (+852) 2517 6912. E-mail: weiranli@hku.hk
[†]Handling Editor: Dr Adam Kent

Estimating mantle temperature is essential for understanding mantle convection and circulation. One route to constraining mantle temperature is via petrological observations, from combining estimates of magmatic temperature with models of melt generation. However, a key factor that has been less emphasised in previous work is the interplay between the temperature of primitive magmas and the composition of the mantle they are derived from. In practice, both of these are unknown and require simultaneous inference from the data. Here we report new estimates of magmatic temperatures for 17 ocean islands and a mid-ocean ridge setting (Siqueiros Fracture Zone) using olivine–spinel thermometry. With the acquired crystallisation temperature estimates, we calculate primary magmatic temperatures using a reverse fractionation model based on the most forsteritic populations of olivine and then apply a multi-lithological mantle melting model to invert for mantle potential temperature (T_p). We find that the most forsteritic olivines investigated in this study have forsterite (Fo) contents between 83.5 and 88.5 and crystallisation temperatures (T_{crys}) between 1130°C and 1340°C (±23–43°C). Calculations using a multi-element diffusion model show that diffusive resetting of olivine Fo content during magma storage may be prevalent under ocean islands. Considering that the observed maximum Fo contents are several units lower than those of the presumed primary mantle olivines (Fo > 90), a correction on $T_{crys}$is required to calculate that of the primary melts and T_p. Here we calculate an olivine-controlled liquid line of descent (LLD) with its one end fixed by the average Fo-T_{crys} (considering possible diffusive resetting) of the most forsteritic population at individual islands, and the other end lying on the (unknown) primary olivine Fo and crystallisation temperature. Mantle potential temperatures calculated from a fixed primary Fo_{91} (=1326–1661°C) show overlap with values reported by previous studies and are regarded as reliable temperature estimates. Using $T_p = 1350$ (±12) °C calculated for Siqueiros using the same approach (but with additional constraints from crustal thickness and magma chemistry), we obtain the plume excess temperature ΔT_p for ocean islands with high-Fo olivines (Fo > 85) as −23°C to 202°C, which are comparable with results reported by recent seismic tomography studies and show correlations with plume buoyancy fluxes from the literature (especially at hotspots providing olivines Fo > 87). We obtain ΔT_p=229–311°C for localities having lower olivine Fo (83–85), which likely indicates an overestimation of plume temperatures. The petrological approaches in this study can be applied to other ocean islands to constrain mantle temperature and identify key geophysical and petrological constraints that may contribute to more reliable mantle temperature estimates in future.

Key words: Diffusion; geothermometer; mantle plume; ocean island; olivine; thermodynamics

INTRODUCTION

Large-scale mantle convection in the Earth is characterised by cold downwellings at subduction zones and upwellings, which often manifest as hotspot-fed ocean islands. The key to understanding the upwelling of mantle plumes is identifying the origin of their positive buoyancy that makes them ascend through the mantle. In this study, we focus on applying petrological methods to constrain the temperature and lithology of the mantle beneath ocean islands, which collectively are the key terms defining their buoyancy.

As the term 'hotspot' would imply, ocean islands are settings that have long been considered to be underlain by anomalously hot, and therefore, buoyant and upwelling regions of mantle (e.g. Morgan, 1971). However, compositional anomalies in the mantle have also been identified as contributing to magmatism at these settings (e.g. Asimow & Langmuir, 2003; Sobolev *et al.*, 2005). One way of accessing information on ocean island mantle temperature is through their magmas, the temperature of which in principle relates to the temperature of their mantle source regions. A priori, we typically know neither the composition nor temperature of the mantle source from which melts are extracted beneath an ocean island. When applying petrological thermometers to constrain the thermal properties of the mantle, we therefore, need to consider its compositional characteristics at the same time. Mantle

RECEIVED JULY 18, 2024; **REVISED** FEBRUARY 2, 2025; **ACCEPTED** MARCH 9, 2025

temperature affects the relative contributions of mantle lithologies to melt production, as hotter mantle will lead to more melting of the refractory lithologies it carries during decompression (e.g. Shorttle *et al.*, 2014), while mantle composition in turn affects the thermal structure of the melting region, as the depth of solidus intersection and melt productivity impact the rate of cooling during decompression (e.g. Phipps Morgan, 2001).

Attempts have been made to combine petrological estimates of mantle temperature with models of how heat is consumed during melting of mantle with fusible and refractory components (e.g. Shorttle *et al.*, 2014; Matthews *et al.*, 2016; Wong *et al.*, 2022). These studies have focused on regions with good constraints on overall melt production, melt region geometry (regions of dominantly passive plate spreading), the lithologies contributing to the aggregate melt, and the petrology of the most primitive magmas entering the volcanic systems. With these combined constraints, simultaneous estimates of mantle composition (the relative proportion of assumed lithologies) and mantle temperature can be obtained (e.g. Matthews *et al.*, 2021).

Considering the case of a general ocean island, however, the constraints on melting, melt composition, and the characteristics of primitive melts and the mantle source are typically weaker than for Iceland and mid-ocean ridges (e.g. Matthews *et al.*, 2021). In the limiting (albeit, common) case, the only available constraint might be the petrological estimate of magma temperature in a moderately evolved melt. In these cases, there are several important assumptions and steps that must be taken to acquire an estimate of mantle temperature from a magma temperature. These steps propagate an uncertainty, and potential degeneracy, in estimating mantle temperature from petrological temperature estimates alone (e.g. Matthews *et al.*, 2021), placing important limitations on our ability to inform models of Earth's interior dynamics.

In this study we investigate how precisely mantle plume temperature can be estimated given only constraints on their magmatic temperatures. We provide new petrological estimates of magmatic temperatures from 17 ocean islands (including 15 ocean islands with geochemical data acquired in this study, and Hawai'i and Iceland with data reported by previous studies). These temperature estimates are derived from compositional measurements of coexisting olivine–spinel pairs using a recently revised olivine–spinel thermometer. We use a multi-element diffusion model to evaluate the degree of diffusive resetting in olivines from this study and take the most forsteritic subpopulations to estimate the temperature of primary magmas. We then employ a multi-lithological mantle melting model to identify the mantle temperatures and lithologies that can produce such melts. Our results focus on the uncertainties propagated through the modelling from applying these methods to only partially characterised systems. The analytical methods, olivine–spinel thermometry equations, and mantle melting model used in this study are detailed below.

SAMPLE INFORMATION AND ANALYTICAL METHODS

Most ocean island samples in this study are from the Harker collection of the Sedgwick Museum, University of Cambridge, and collections of the National History Museum in London; the Galápagos samples are provided by D. Geist, and one sample from Piton de la Fournaise, Réunion was reported in Salaün *et al.* (2010). The rocks are mainly basalt/olivine basalt (see sampling locations and other information in Supplementary Table S1). For each ocean island, we took at least one rock sample from a single volcanic system and either crushed the rocks and mounted the picked olivine single grains in epoxy resins or cut the rocks to make thin sections for the consequent electron microprobe analysis.

The ocean island olivine crystals and their spinel inclusions were analysed in four sessions between June and November 2021, using a Cameca SX100 electron microprobe at the Department of Earth Sciences, University of Cambridge. We acquired $n = 322$ and $n = 246$ analyses for olivine and spinel respectively from 124 olivine–spinel pairs (see Supplementary Tables S2 and S3), with analytical conditions described below.

Olivine crystals were analysed using an accelerating voltage of 15 kV under two different analytical conditions: a standard beam current (20 nA) for Mg, Si, Fe and Ti, and a higher beam current (100 nA) with a longer counting times for other elements (Al, Ca, P, Cr, Mn, Ni) (see primary standards and counting times in Supplementary text and Table S4). To acquire high precision Al measurements for the subsequent thermometric calculations, Al in olivine was analysed using two spectrometers (with TAP and LTAP crystals, respectively), with a long acquisition time of 150 seconds on each. Spinel inclusions were analysed using a voltage of 15 kV and a beam current of 40 nA. About 3 to 5 measurements were conducted on each olivine/spinel crystal. The positions of measurements in olivine were chosen to be about 30 to 50 μm away from the spinel inclusion(s) to ensure that the two phases are likely to have been in thermodynamic equilibrium at the time of spinel entrapment, while minimising the interference of Al and Cr in spinel on the analysis of olivine. Three secondary standards were analysed every 6 to 8 hours in between the unknowns, including two olivine standards (in-house San Carlos, and MongOL sh11–2 of Batanova *et al.*, 2019) and one chromium augite standard (NHNM164905) (see the accuracy and precision derived from the analysis of secondary standards in Supplementary Table S4 and Fig. S1). Repeated measurements of Al_2O_3 in MongOL ($n = 153$) and San Carlos ($n = 95$) olivines showed a 1 s.d. precision of 14 ppm (2.9%, relative) and 23 ppm (5.6%, relative), respectively, whereas the counting statistics indicate an uncertainty of ~25 ppm in Al, which is propagated to the error in the calculated T_{crys}.

OLIVINE–SPINEL COMPOSITIONS AND CRYSTALLISATION TEMPERATURES

Olivine and spinel compositions

The ocean island basalt (OIB) olivines in this study have Fo contents between 78 and 89 and Al concentrations between 140 and 380 ppm (Fig. 1), where Fo and Al contents generally show a positive correlation, although at some locations a large variation in Al is seen within a narrow range of Fo content (e.g. Galápagos). The OIB olivines have a similar average Al content (239 ppm) as the global OIB olivine in the GEOROC database ($n = 2524$; mean: 229 ppm Al). The Al contents of high-Fo OIB olivines (Fo = 85–89) mostly overlap with those of similar Fo contents from Iceland (Matthews *et al.*, 2016; Spice *et al.*, 2016), except that olivines from Crozet and Azores show Fo–Al contents similar to those from the Siqueiros Transform (Coogan *et al.*, 2014; Matthews *et al.*, 2021) (Fig. 1). Variations in Al–Mn–Ni–Ca with Fo contents of olivines in this study are shown in Supplementary Materials (compilation of all data in Figs S3 and S4; data for individual islands in Figs S6–S10; full dataset in Table S2).

The OIB spinel in this study have Cr# of 0.29 to 0.68 and Mg# of 0.38 to 0.69 ($Mg\# = \frac{[Mg]}{[Mg]+[Fe^{2+}]}$, square brackets denote mole

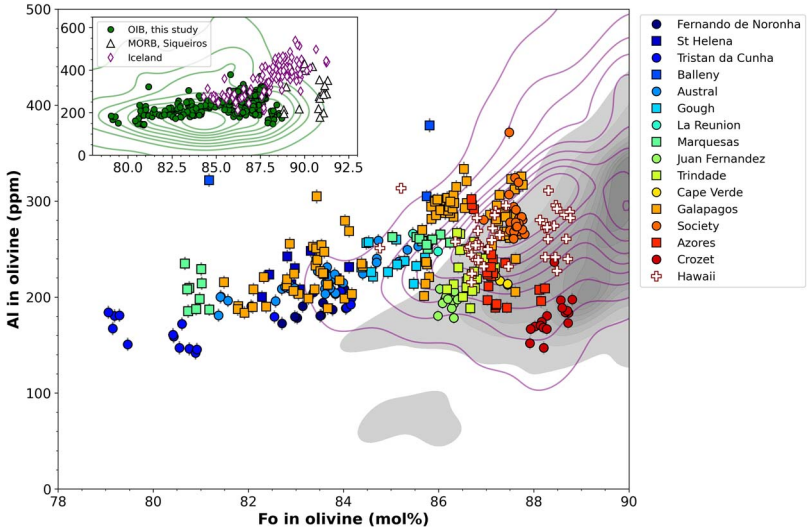

Fig. 1. Forsterite (Fo) and Al contents of OIB olivine from this study (ocean islands in the figure legend are sorted in ascending order by their average Fo content of the most forsteritic sub-population of olivine). Olivine data previously reported for Hawai'i (Kama'ehuakanaloa and Kīlauea; Matthews *et al.*, 2021), Iceland (Matthews *et al.*, 2016; Spice *et al.*, 2016), and Siqueiros (Coogan *et al.*, 2014; Matthews *et al.*, 2021) are plotted as different symbols filled in white (see legend). A compilation of data for global OIB olivines adopted from GEOROC database are plotted in the inset (see contours). Data compiled by Sobolev *et al.* (2007) for MORB and Iceland olivines are shown in shaded areas and contours, respectively in the main plot. Uncertainties in the measured olivine Fo-Al concentrations are shown in grey error bars (some are smaller than the symbols).

fraction), overlapping with those from Siqueiros (Coogan *et al.*, 2014; Matthews *et al.*, 2021) and Iceland (Matthews *et al.*, 2016; Spice *et al.*, 2016). The Al–Cr–Fe^{3+} ternary diagram in Fig. 2 shows that most OIB spinel fall into the compositional range of experimental products that were used to calibrate the thermometer equations; some contain high Fe^{3+} similar to that in spinel from large igneous provinces (LIPs) (Cheng *et al.*, 2020; Heinonen *et al.*, 2015; Jennings *et al.*, 2019; Spice *et al.*, 2016; Trela *et al.*, 2017; Wu *et al.*, 2022; Xu & Liu, 2016; Zhang *et al.*, 2021) but much higher than that in spinel from MORB and Iceland.

Olivine crystallisation temperature T_{crys}

Calculation using olivine–spinel thermometer equations

Olivine crystallisation temperature (T_{crys}) can be calculated from thermometers assuming thermodynamic equilibrium between olivine and liquid (e.g. Putirka *et al.*, 2007; Pu *et al.*, 2017), or olivine and other minerals (e.g. spinel; Wan *et al.*, 2008; Coogan *et al.*, 2014). The latter type of thermometers has the advantage of not requiring a liquid composition which is usually unknown. In particular, the olivine–spinel Al exchange thermometer that we use in this study can be regarded as a reliable method due to slow diffusion rates of Al in olivine hindering syn-/post-crystallisation diffusive resetting at magmatic temperatures. Considering this, we use olivine–spinel thermometers to calculate olivine crystallisation temperatures. Specifically, we take the thermometer equations of Zhang *et al.* (2023) that were calibrated from an experimental dataset including new experimental data and data from the literature. The dataset spans a wide range of *P*–*T*-composition conditions (1174–1606°C, 0.1–1350 MPa, up to 7.4 wt % water) and covers spinel compositions of most OIB samples (see the Al–Cr–Fe^{3+} ternary diagram in Fig. 2). With this dataset three different thermometer equations were proposed, all involving olivine–spinel Al exchange but some involving additional elements in spinel. We chose to use two equations of Zhang *et al.* (2023) as follows.

The first thermometer equation we use is in the same format as the Al-exchange equation of Coogan *et al.* (2014) but with updated

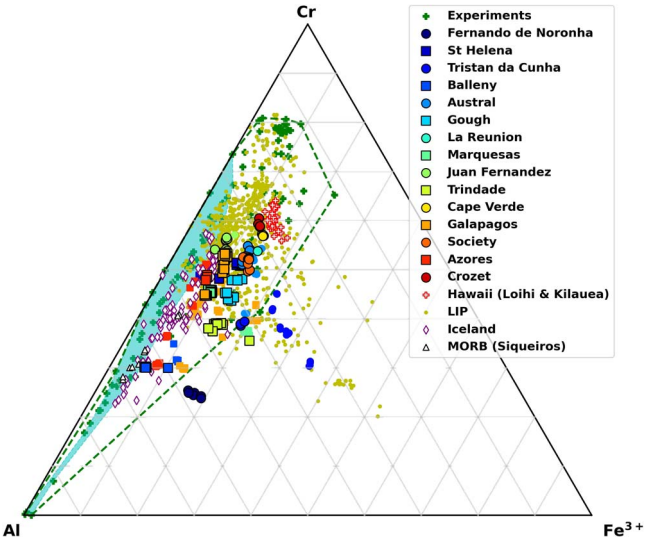

Fig. 2. An Al–Cr–Fe^{3+} ternary diagram showing spinel compositions in OIBs from this study (those used to calculate T_{crys} marked in symbols with black outlines) and those reported by previous studies for Siqueiros (Coogan *et al.*, 2014), Hawai'i (Matthews *et al.*, 2021), Iceland (Matthews *et al.*, 2016; Spice *et al.*, 2016), and large igneous provinces (Heinonen *et al.*, 2015; Spice *et al.*, 2016; Xu & Liu, 2016; Trela *et al.*, 2017; Jennings *et al.*, 2019; Cheng *et al.*, 2020; Zhang *et al.*, 2021; Wu *et al.*, 2022). Experimental spinels used to derive olivine–spinel thermometers are within the compositional range marked in dashed line (solid cross: data from Zhang *et al.*, 2023; shaded area: data from Coogan *et al.*, 2014 and references therein). Uncertainties in the spinel compositions are smaller than the symbols.

coefficients, written as:

$$T_{crys}\,(\mathrm{K}) = \frac{10,000}{0.740\,(\pm0.317) + 1.144\,(\pm0.136)\,\mathrm{Cr\#} - 0.865\,(\pm0.046)\ln \mathrm{K_d\,(Al)}}, \quad (1)$$

where $\mathrm{K_d(Al)} = \frac{c^{ol}_{Al}}{c^{sp}_{Al}}$ (c denotes weight concentration), and spinel $\mathrm{Cr\#} = \frac{[Cr]}{[Cr]+[Al]}$ (square brackets denote mole fraction). The second thermometer equation we use accounts for the effect of non-ideal

mixing in spinel (e.g. Sack & Ghiorso, 1991a, 1991b), expressed with an additional compositional variable (φ^{Spl}) as:

$$T_{crys}\,(\mathrm{K}) = \frac{10000\varphi^{Spl}}{-0.168\,(\ln \mathrm{K_d}\,(\mathrm{Al})) + 0.654}, \quad (2)$$

where φ^{Spl} is determined by multiple components in spinel, including Mg, Fe^{2+}, Fe^{3+}, Cr, and Ti (see Equation (6) of Zhang *et al.*, 2023 for details). The spinel Fe^{3+} contents were calculated following Droop (1987), i.e. using stoichiometric criteria assuming that iron is the only element present with variable valency and that oxygen is the only anion. Errors in Fe^{3+} are estimated to be mostly <20% (relative), considering analytical errors in all elements used in stoichiometric calculation. The uncertainty (1σ) on Equations (1) and (2) were calculated by Zhang *et al.* (2023) from a test set of the experimental data to be ±43.3°C and ± 23.9°C, respectively. These are the main source of error in the T_{crys} reported in this study because they are significantly larger than errors inherited from electron microprobe analyses (± 5–7°C). The overall error calculated from combining errors on the thermometer equations and the analyses, using $\sigma_{overall} = \sqrt{\sigma^2_{equation} + \sigma^2_{analysis}}$, is only slightly (0–2°C) higher than errors induced by the thermometer equations alone. Compared to Equation (1), Equation (2) contains more parameters, is thermodynamically more complete, and shows a smaller uncertainty in the fit to the experimental data, but it is less resistant to diffusive resetting because it involves Mg–Fe in spinel. We did not use the other equation of Zhang *et al.* (2023) involving Cr in olivine (i.e. their Equation (8)) for two reasons: (i) the measurements of low Cr contents (down to ∼0.01 wt.%) in the OIB olivines from this study have considerable errors (14–17% relative; Table S4) that can induce large uncertainties on the T_{crys}, and (ii) taking this equation along with the other two will only change ∼9% of the T_{crys} reported in this study by a median of ∼9°C (±8°C) (Supplementary Fig. S16).

Selection of calculated crystallisation temperature

We use Equations (1) and (2) to calculate T_{crys}(denoted as T_{crys}[Eq.(1)] and T_{crys}[Eq.(2)] hereafter) for $n = 1278$ pairs of olivine–spinel (each measurement on olivine and on its spinel inclusion regarded as one pair). The T_{crys} calculated from the two equations are shown in Fig. 3 for cross comparison and reported in Table S5. The T_{crys}[Eq.(1)] are mostly (∼97%) higher than T_{crys}[Eq.(2)], with an increasing difference towards less forsteritic olivine (some exceeding the uncertainty inherent to the thermometer equations by >100°C; see all data in Fig. 3c and data for individual islands in Supplementary Fig. S15). The T_{crys}[Eq.(2)] generally follow the trend of an LLD with olivine fractionation (Fig. 3b). This is unexpected for low-Fo olivines (e.g. Fo ≈ 80) because with olivine fractionation, other phases (e.g. clinopyroxene ± plagioclase) may crystallise concurrently and produce a LLD of smaller gradients (in Fo-temperature space) than olivine-only fractionation (e.g. Ghiorso, 1997). This implies that some of the T_{crys}[Eq.(2)] calculated for low-Fo olivines might be somewhat underestimated, possibly due to the progressive diffusive resetting of olivine–spinel pairs towards lower temperature equilibria upon magma evolution. This can be recorded by the fast diffusing components (e.g. Fe–Mg) in Equation (2), which are not in Equation (1), therefore, the latter tends to provide higher T_{crys}. Given the possible underestimation but higher precision of T_{crys}[Eq.(2)], we select the results based on the difference in T_{crys} between the two equations ($\Delta T_{crys} = T_{crys}$[Eq.(1)] − T_{crys}[Eq.(2)]) and a statistical *Z*-test following Zhang *et al.* (2023), which is detailed below:

(a) when $\Delta T_{crys} \geq 0$ (i.e. T_{crys}[Eq.(1)] ≥ T_{crys}[Eq.(2)]), the value of T_{crys}[Eq.(2)] may be decreased by diffusive re-equilibration, and a *Z*-test is conducted to compare ΔT_{crys} with uncertainties (σ) in the two thermometer equations, using $Z = \frac{\Delta T_{crys}}{\sqrt{\sigma^2_{Eq.1} + \sigma^2_{Eq.2}}}$ (where the denominator equals to ∼50°C). The ΔT_{crys} and *Z* values determine whether the difference between the two thermometer equations is *significant*:

(a.1) if $Z > 1.35$ ($\Delta T_{crys} > 67$°C), the difference is *significant*. This likely indicates diffusive reequilibration that lowers T_{crys}[Eq.(2)], so we take T_{crys}[Eq.(1)]. About 38% of the results (mainly from olivine Fo < 85) fall into this scenario and show higher T_{crys}[Eq.(1)] than T_{crys}[Eq.(2)] (by up to ∼770°C) (Supplementary Figs S15 and S16).

(a.2) if $Z \leq 1.35$ ($0 \leq \Delta T_{crys} \leq 67$°C), the difference is *insignificant*, so we take T_{crys}[Eq.(2)] with a smaller uncertainty. About 59% of the results fall into this scenario.

(b) when $\Delta T_{crys} < 0$ (i.e. T_{crys}[Eq.(1)] < T_{crys}[Eq.(2)]), the value of T_{crys}[Eq.(2)] was unlikely to be decreased by diffusive resetting, so we take T_{crys}[Eq.(2)] due to its smaller uncertainty. Only ∼3% of the results (two olivine crystals from Azores and one crystal from Trindade) fall into this scenario, showing ΔT_{crys} between −5°C and 0°C.

We find that individual crystals mostly fall into a single scenario (see selected values from Z-test in Table S5), except three crystals (two from Austral and one from Society) providing values in either scenario (a.1) or scenario (a.2). This is because the ΔT_{crys} calculated from multiple measurements on the same olivine crystals vary around the threshold value of ∼67°C. Here we took the T_{crys} produced by the dominant thermometer equation determined by the *Z* test for the three crystals (see the chosen T_{crys} in Table S5). This correction caused small changes in the average T_{crys}, i.e. by +16°C for Austral (=1247°C) and −6°C for Society (=1227°C). Compared to other ocean islands, the olivine from Borgarhraun, Iceland shows relatively small ΔT_{crys} (−31 to 13°C) within the equations' uncertainties (∼90% in scenario (b) and ∼10% in scenario (a.2)). The olivine from Siqueiros shows ΔT_{crys} between −22°C and − 12°C (all in scenario (b)), likely indicating a negligible effect of diffusive resetting which is distinct from most ocean islands in this study. Overall, the protocol above provided T_{crys}=1118–1340°C (±24–44°C) for the 16 ocean islands in this study, 1146°C to 1376°C for Borgarhraun, and 1165°C to 1295°C for Siqueiros (Fig. 3c).

LINKING CRYSTALLISATION TEMPERATURES TO MANTLE POTENTIAL TEMPERATURE

To link olivine crystallisation temperatures to mantle potential temperature (T_p), one must consider the heat consumption during mantle melting and olivine fractionation (Fig. 4). This can be divided into three stages from the source mantle to the crust: (1) adiabatic melting of the mantle, which starts when the geotherm intersects with the source lithology solidus and ceases at the base of the lithosphere (for intra-plate ocean islands) or of the crust (for mid-ocean ridges); (2) extraction of primitive liquids from the base of the lithosphere (or crust) and olivine saturation at a given T (T^{prim}_{crys}) and depth in the crust; and (3) fractionation that produces olivine of Fo contents lower than the primitive olivine at T_{crys}, which we can calculate from olivine-based thermometers. Stages (1) and (2) were handled with methods from previous studies summarised in this section, whereas stage (3) was quantified

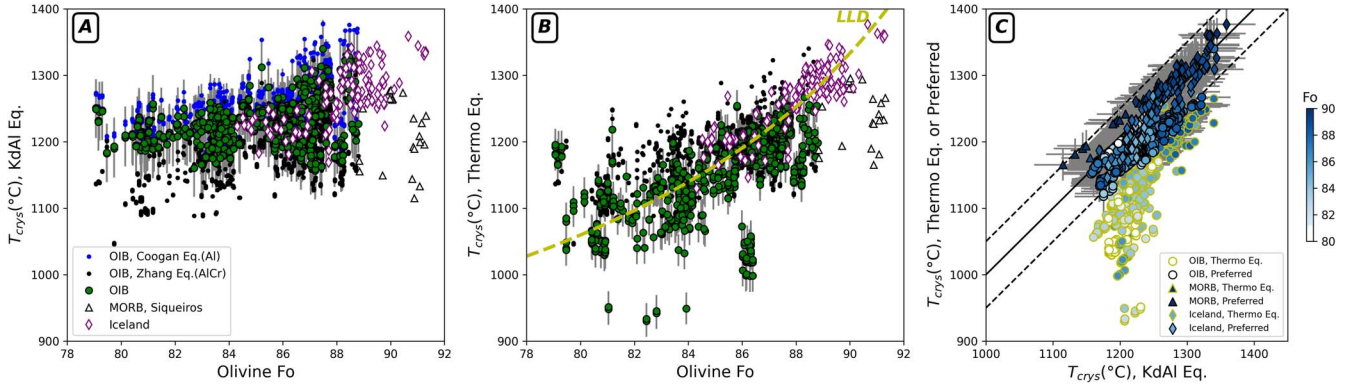

Fig. 3. Olivine Fo (mol%) plotted versus crystallisation temperatures T_{crys} obtained by the Al-exchange based Eqn. (1) and thermodynamics based Eqn. (2) of Zhang *et al.* (2023) (panels *a*, *b*). The values selected from the two equations (symbols with black outline in panel c) are subject to recovering the statistically highest temperature (see main text). For most results from Eqn. (2) (panel *b*), the variation in T_{crys} with Fo follows the trend of an olivine-only LLD, rather than one where multiple mineral phases are saturated, which is a likely scenario for the low-Fo olivine (see text). More than half of the T_{crys} values calculated from the two equations overlap within each other's uncertainty, but some from Eqn. (2) (symbols with coloured outlines) are significantly lower (likely due to diffusive reequilibration) and are not taken as recommended values (see text). Error bars show uncertainties in T_{crys} accounting for those in the thermometry equation and electron microprobe analysis (1σ).

using models developed in this study and detailed in the following section.

Stage 1: Adiabatic mantle melting

The consumption of latent heat during mantle melting is constrained following Matthews *et al.* (2021), using an adiabatic mantle melting model (pyMelt; Matthews *et al.*, 2022) accounting for a non-melting lithology (refractory harzburgite described in Shorttle *et al.*, 2014), and two melting lithologies, i.e. the KLB-1 lherzolite of Davis *et al.* (2009), and the KG1 silica-undersaturated pyroxenite of Kogiso *et al.* (2004) (representing a 1:1 mixture of KLB-1 lherzolite and average MORB). The choice of pyroxenite KG1 was justified in Shorttle and Maclennan (2011) for Iceland where the compositions of enriched melts are best matched by melting of this pyroxenite. The same pyroxenite was adopted in our calculation but we note that possible variations in the pyroxenite composition between localities may induce additional uncertainties in the model results. For ocean islands, there are three input parameters for the forward modelling, i.e. T_p and the fractions of pyroxenite (φ_{px}) and harzburgite (φ_{hz}) (the fraction of lherzolite is dependent on these two given that $\varphi_{lz} = 1 - \varphi_{px} - \varphi_{hz}$). With each set of T_p, φ_{px} and φ_{hz}, the mantle melting model predicts the geothermal gradient, total melt fractions (F), and melt fractions of the pyroxenite (F_{px}) and lherzolite (F_{lz}) (Fig. 4). The deepest position of the melting region is determined by where the geotherm intersects with the pyroxenite solidus, whereas the shallowest position of melting is taken to be at the lithosphere-asthenosphere boundary (LAB, estimated from lithospheric thickness in Table 1) for ocean islands (Fig. 4a) and at the base of the crust for mid ocean ridges (Fig. 4b).

Stage 2: From primitive liquids to primitive olivine crystallisation

The primitive melt extracted from the base of the lithosphere beneath ocean islands continues to cool down during ascent in the crust, following the liquid isentrope (assuming no interaction between the melt and lithosphere). The temperature of olivine saturation is calculated following Matthews *et al.* (2016), using the pressure-dependent olivine-saturation surface equation of Putirka (2008b). Given the Clapeyron slope of the liquidus of 39.16 K/GPa, the variation in pressure (within the crustal level) should have a small influence on the calculated saturation temperature. Here we take an intermediate pressure corresponding to a depth of 14 km (allowing a variation of ±2 km) to calculate olivine saturation temperature. Changing the depth to a higher value (e.g. 20 km) will only produce a slightly lower T_p (e.g. by ~10°C for Hawai'i; see results in Supplementary Materials). The lower value between the olivine saturation temperature and liquid isentrope was then taken as the primitive crystallisation temperature T^{prim}_{crys} to invert for T_p and source lithology fractions.

Stage 3: From crystallisation of primitive olivine to that of the analysed olivine

The olivine grains available in the samples of interest can be much less forsteritic than the primitive olivine, thus recording lower crystallisation temperatures. This is evident in the pre-compiled olivine compositions from GEOROC database showing that the highest Fo contents found for global ocean islands range from 80 to 92.3 (median: 87.8). Given the highest olivine Fo of 84–89 in this study, the T_{crys} we calculated could be a lot less than T^{prim}_{crys}; therefore, the difference between them must be considered to estimate T^{prim}_{crys} and T_p. The approaches we use to estimate T^{prim}_{crys} are detailed in the following section.

ESTIMATING PRIMITIVE OLIVINE CRYSTALLISATION TEMPERATURES

The crystallisation temperature of primitive olivine on the same LLD as the analysed olivine can be estimated using an 'olivine addition' method as follows (see detail in Supplementary Materials and python codes in a Zenodo repository; Li, 2025). Instead of taking a guessed primitive liquid composition which is poorly known, we start the calculation with the analysed forsteritic olivine. The mole fraction of Mg–Fe in the starting liquid, in equilibrium with the chosen olivine at given Fo–T_{crys}, were estimated using the partition coefficient for Mg (D_{Mg}) calculated from Equation (2) of Putirka *et al.* (2007) and an exchange coefficient for Fe–Mg $Kd^{ol-liq}_{Fe^{2+}-Mg}$ of 0.3 ± 0.03 (Roeder & Emslie, 1970). A small amount of olivine in equilibrium was then added to this liquid to generate a new melt, and the temperature was re-calculated using the equation for D_{Mg} mentioned above. This calculation was repeated till reaching a given olivine Fo_{prim} to obtain T^{prim}_{crys}.

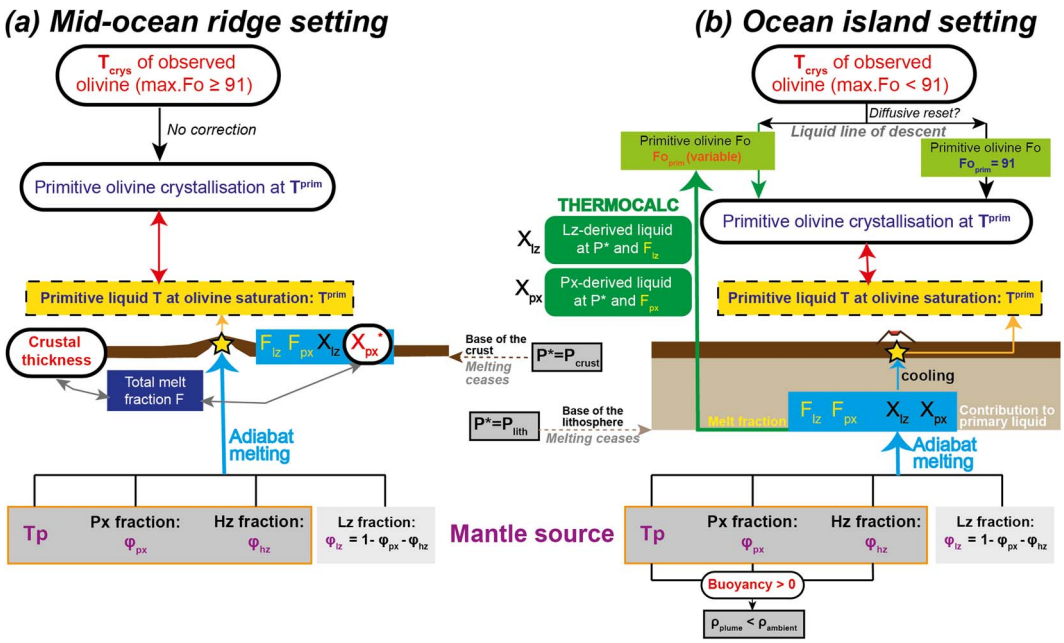

Fig. 4. A flow chart of modelling approaches used in this study, with the difference in the approach applied to mid-ocean ridge (MOR) and ocean island (OI) settings highlighted. Posteriors of the mantle melting model are mantle potential temperature (T_p) and source lithology fractions (φ with different subscripts for different lithologies, '*lz*' = lherzolite, '*px*' = pyroxenite, '*hz*' = harzburgite; φ_{lz} is dependent on φ_{px} and φ_{hz} as they sum to unity). The melt fractions of the pyroxenite (F_{px}) and lherzolite (F_{lz}) are calculated with the geotherm. For ocean islands, the predicted F_{px} and F_{lz} and the proportions of pyroxenite- and lherzolite-derived melts (X_{px}, X_{lz}) were used to calculate T_{prim}. For Siqueiros and Iceland, the contribution of pyroxenite-derived melts to the volume of the crust (X_{px}*) was estimated in previous studies (see main text) and used as an additional constraint of F_{px} and thus T_p in the inversion model.

Table 1: Parameter values used to calculate mantle potential temperatures

Location	Island	Fo, mean	1σ	T_{crys} (°C), mean	1σ†	t_{lith} (km)‡	t_{crust} (km)	X_{px}*
Azores	Flores	88.2	0.1	1170	24	36 ± 5	14 ± 2	-
Balleny	Borradaile	85.3	0.8	1217	49	60 ± 5	14 ± 2	-
Cape Verde	São Vincente	87.3	0.1	1191	24	95 ± 5	14 ± 2	-
Crozet	Possession	88.2	0.2	1165	33	83 ± 5	14 ± 2	-
Fernando de Noronha	-	83.5	0.4	1182	45	89 ± 5	14 ± 2	-
Galápagos	near Fernandina	87.5	0.2	1223	31	55 ± 5	14 ± 2	-
Gough	-	85.1	0.4	1229	45	58 ± 5	14 ± 2	-
Hawai'i	Kama'ehuakanaloa	88.5	0.2	1285	44	75 ± 5	14 ± 2	-
Juan Fernandez	-	86.3	0.1	1198	44	55 ± 5	14 ± 2	-
Réunion	-	85.7	0.4	1211	24	70 ± 5	14 ± 2	-
Marquesas	-	85.7	0.3	1188	25	75 ± 5	14 ± 2	-
Society	Tahiti	87.6	0.1	1227	27	86 ± 5	14 ± 2	-
St. Helena	-	83.9	0.2	1224	44	61 ± 5	14 ± 2	-
Trindade	-	86.8	0.3	1183	32	86 ± 5	14 ± 2	-
Tristan da Cunha	-	84.1	0.1	1205	44	50 ± 5	14 ± 2	-
Borgarhraun, Iceland*	-	91.1	0.3	1363	24	-	20 ± 1	0.3 ± 0.1
Siqueiros (MOR)*	-	91.0	0.2	1226	34	-	5.74 ± 0.27	0.175 ± 0.1

*The values of input parameters used in the calculations for Siqueiros and Iceland were adopted from Matthews *et al.* (2021). Note that different parameters were used in the calculations for mid-ocean ridge and ocean island settings (see Fig. 4). †Combined uncertainties considering those in the thermometer equations and the standard deviation of the selected forsteritic olivine (see Table S6). ‡The lithospheric thickness estimates for the ocean islands were adopted from Dasgupta *et al.* (2010) except for the following: Balleny from An *et al.* (2015), Galápagos from Gibson and Geist (2010), Hawai'i from Matthews *et al.*, (2021) Réunion from Fontaine *et al.* (2015), and Marquesas and St. Helena from Humphreys and Niu (2009).

The calculated T_{crys}^{prim} at Fo_{prim}=91 are reported in Table 1 (see calculated primary liquid compositions in Table S6). The two endpoints of the LLD (i.e. the Fo content and T_{crys} of the analysed olivine, and the Fo_{prim}) determine the calculated T_{crys}^{prim} and are described separately in this section.

Determining the evolved starting point of the reverse LLD

An olivine-only LLD assumes that the melt is saturated in olivine only, which may not be true (especially at low olivine Fo where other phases, such as clinopyroxene ± feldspars can be saturated) and may generate olivine Fo-temperature gradients different from those considered in the approach we use (Ghiorso, 1997). Considering this, we take the most forsteritic sub-populations of olivine from individual ocean islands to estimate T_{crys}^{prim}. We determine the most forsteritic sub-populations by conducting clustering analyses of olivine compositions using a k-means clustering algorithm (in Python *sklearn* library), instead of arbitrarily taking a threshold Fo content. Clustering analysis using the pairs of olivine Fo and any single element among Al–Ni–Ca–Cr–Mn produces identical

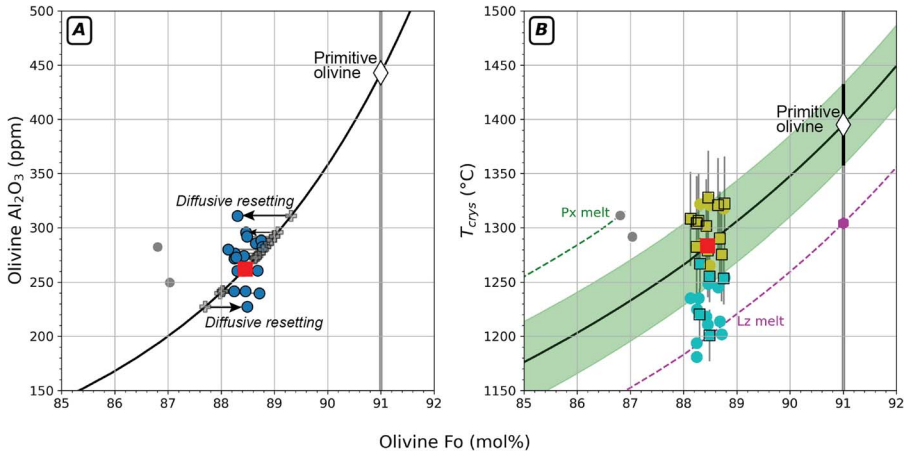

Fig. 5. Calculation of T^{prim}_{crys} using olivine crystallisation temperatures considering fractionation and diffusive resetting. The olivine from Kama'ehuakanaloa, Hawai'i reported by Matthews *et al.* (2021) are taken as examples in this plot. Panel (*a*) shows the Fo-Al contents of olivine (the most forsteritic sub-population: coloured dots; data showing lower Fo: grey dots; uncertainties in the olivine compositions are smaller than the symbols), and a liquid line of descent (LLD; dark line) that passes through the average composition of the high-Fo sub-population (solid squares), assuming the present distribution is modified (via diffusion; see the trend marked in arrows) from an initial distribution following the LLD. Panel (*b*) shows the T_{crys} calculated using Eqns. (1) and (2) (in yellow and cyan circles, respectively) and the preferred values (symbols outlined with black squares). The T^{prim}_{crys} derived from the LLD at Fo_{91} is marked in white diamond (uncertainties in temperatures shown in error bar and the green band). The LLDs derived from lherzolite and pyroxenite are marked in dashed lines.

results. The number of clusters (n) was set to be the smallest integer covering the observed Fo interval (where $1 \leq n \leq$ total number of olivine grains from a given locality). The high-Fo sub-populations identified for individual ocean islands were used to calculate T^{prim}_{crys} (see Supplementary Fig. S15).

After identifying the high-Fo sub-populations, the next step is to assess whether they were generated by olivine-only fractionation or were affected by magma mixing and/or diffusive resetting (e.g. Matthews *et al.*, 2021; illustrated in Fig. 5b). Effects of different processes on olivine composition are described below:

(i) Mixing of primary liquids derived from lherzolite and pyroxenite, having higher **Mg#** and lower Mg# (e.g. Jennings *et al.*, 2016), will produce olivine of higher Fo and lower Fo contents respectively, at the same temperature. Therefore, a pure lherzolite-derived melt may be responsible for the lowest T_{crys} of the forsteritic population of olivine, which in turns will yield a minimum estimate of T^{prim}_{crys}.

(ii) Diffusive resetting of olivine compositions in a mush pile prior to eruption (e.g. in Iceland; Thomson & Maclennan, 2013). Since Fe–Mg diffuse a few orders of magnitudes faster than Al in olivine (e.g. see Chakraborty (2010) and references therein), the Fo content of olivine may be reset relatively quickly whilst the Al contents are less affected, hence the estimates of T_{crys} based on Al exchange between olivine–spinel reported in this study. Considering the effect of diffusive resetting on reducing the compositional variability towards an intermediate Fo content, it is appropriate to take the average Fo–T_{crys} of the forsteritic population of olivine as an approximation of the pre-diffusion values.

Although it is difficult to assess the effect of scenario (i) without further geochemical characterisation of the samples, it is possible to evaluate the effect of scenario (ii) which we attempted in this study. Here we use a numerical model to simulate the fractionation- and diffusion-induced variability of multi-elements (Fe–Mg, Mn, Ni, Cr, Ca, Al) concentrations in olivine and compare the model fits to the observation to assess the effect of diffusive resetting on the observed olivine composition. The approach is detailed below.

Prediction of olivine composition produced by fractionation

Variations in olivine composition during olivine-only fractionation were calculated in a similar manner to the 'olivine addition' method mentioned above, i.e. exempting prior knowledge of the primitive liquid composition. For any component i among Fo, Mn, Ni, Cr, Ca, Al, the evolved endpoint of the LLD in Fo-i space is forced to be at the average of the high-Fo sub-population (Fig. 6A). The composition of the starting liquid was calculated using partition coefficients D_i^{ol-liq} $(=\frac{X_i^{olivine}}{X_i^{liquid}})$ for Mn, Ni, Cr, Ca, and Al, where we take the equations of Herzberg & O'hara (2002) having D_{MgO}^{ol-liq} as the only variable (see equations in Supplementary Materials, Section 3). With the available equations for these elements, we can investigate the temperature effect for Ni by comparing the results above with those calculated using a T-dependent equation of Matzen *et al.* (2017), i.e. $D_{Ni}^{ol-liq} = \exp\left(\frac{4505\pm196}{T} - 2.075 \pm 0.120 - \ln D_{MgO}^{ol-liq}\right)$. The two different equations yield similar Ni concentrations in olivine (see Supplementary Figs S8 and S9). Therefore, we only take the equations of Herzberg and O'hara (2002) to calculate the partition coefficients for Mn, Ni, Cr, Ca, and Al for the sake of consistency. With the starting liquid composition, we added a small amount of olivine in equilibrium with it to generate a new melt and new olivine and repeated this calculation till reaching the selected Fo_{prim}. With each modelled LLD, an array of concentration was produced for each component (Fo, Mn, Ni, Cr, Ca, and Al) and was compared to the observation as follows.

Calculation of covariance and misfits between models and data

To assess how well the fractionation model can reproduce the variance of element concentrations in the analysed olivine, we calculate the covariance of component pairs from observations/models, using the equation below:

$$cov_{A-B} = \frac{\sigma(A) * \sigma(B)}{\mu(A) * \mu(B)}, \quad (3)$$

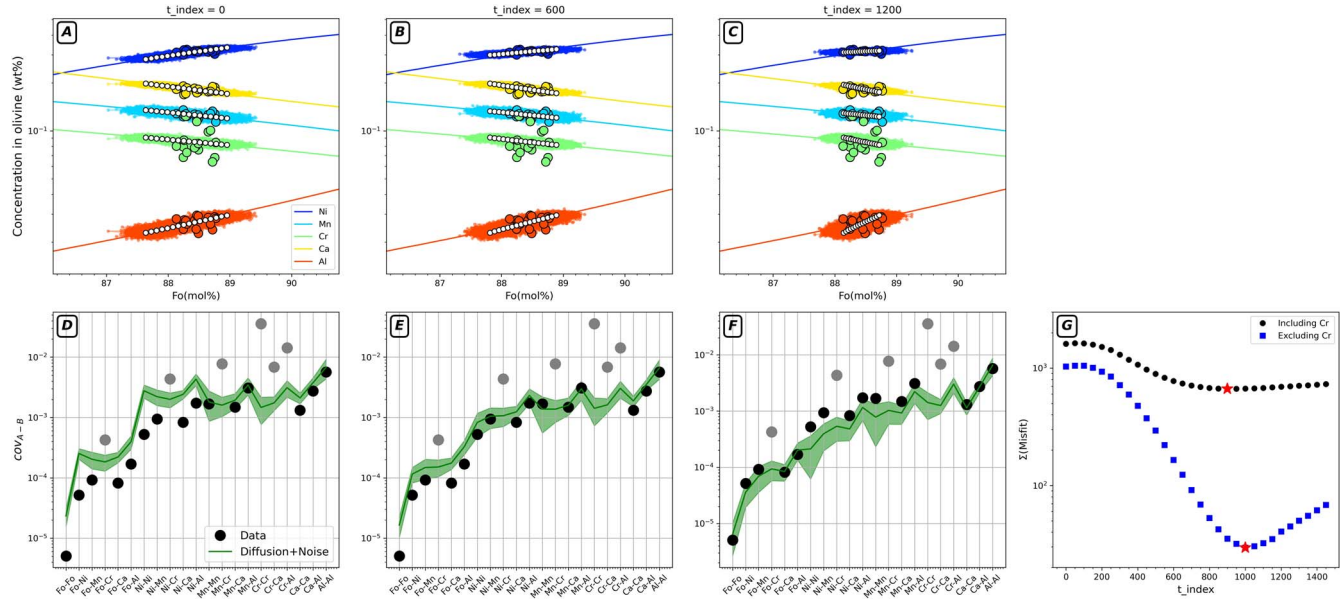

Fig. 6. The measured compositions of olivine from Kama'ehuakanaloa, Hawai'i (concentrations marked in large colourful circles; analytical noise induced by EPMA marked in small colourful dots), and the modelled compositions (circles filled in white) in two different scenarios: (*a*) fractionation, following the LLDs marked in colourful lines, and (*b-c*) fractionation followed by diffusive resetting, where the initial olivine compositions were taken from the fractionation model results in panel (*a*) ('t_index' in the subplot titles represent numbers of iteration of the diffusion models). Note that elements having different diffusion rates show concentration variations by different extents with time. Panels (*d-f*) show the covariance calculated using Equation (3) for the measured (in black circles) and modelled compositions (in solid lines; shaded areas showing uncertainty ranges with analytical errors considered). The Cr-involving pairs (grey circles in panels *d–f*) generally show poorer model fits than other component pairs. Panel (*g*) shows variations in the sum of misfits with diffusion time, which are significantly reduced when the Cr-involving pairs are excluded (coloured squares) than being included (black dots) (minimum Σ(Misfit) marked in red stars).

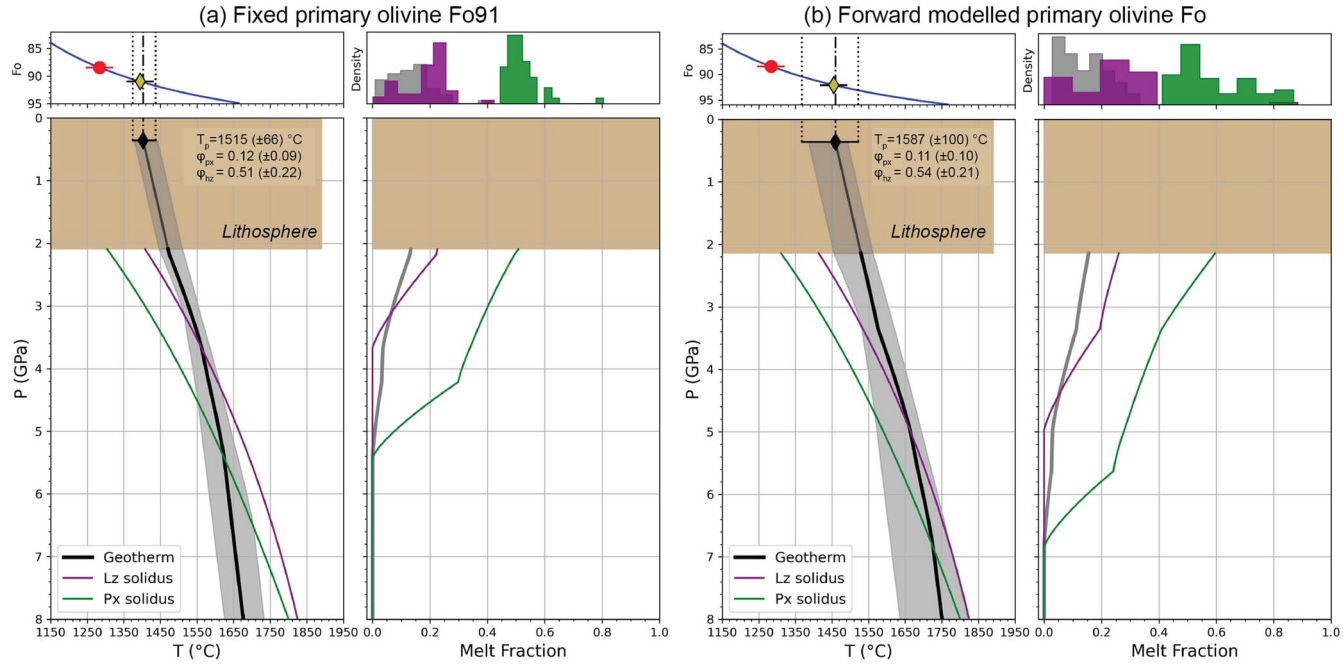

Fig. 7. Illustration of the forward model for Kama'ehuakanaloa, Hawai'i using the median (solid lines) and 68% confidence interval (grey area) of the posterior T_p, φ_{lz} and φ_{px}, calculated using different primary olivine Fo contents: (*a*) a fixed Fo = 91, and (*b*) forward modelled Fo derived from a combination of THERMOCALC and mantle melting modelling (see main text). The T^{prim}_{crys} in the upper panels (yellow diamonds) were calculated by extrapolating an olivine-only LLD (blue lines) from the most forsteritic population of olivine (in solid circles) to given Fo (in diamonds). Note that the T_p and T^{prim}_{crys} (dark diamonds in the lower panels) yielded by the mantle melting model with variable primary olivine Fo (panel *b*) have larger uncertainties than those calculated using Fo_{91} (panel *a*), due to additional uncertainties induced by variations in the source lithology fractions in the former scenario. The geotherm and pyroxenite-lherzolite solidi are shown in black, green and purple lines on the left-hand side of two panels (see legend). The distributions of the total melt fractions and melt fractions of the pyroxenite and lherzolite (predicted by the median of the posterior T_p, φ_{lz} and φ_{px}) are plotted as histograms in grey, green, and purple respectively (variations in these melt fractions with pressure marked in corresponding colours). Diagrams for other ocean islands can be found in Supplementary Materials.

where μ and σ denote mean and standard deviation of the (measured or modelled) concentration of component *A* or *B* (taken from Fo, Mn, Ni, Cr, Ni, and Al). To compare the cov_{A-B} of the measured data with that of the models, we need to consider the same compositional range within that of the high-Fo population of olivine. An intuitive way might be referring to the range of Fo contents from measurements, however, these may have been changed by diffusive resetting to be smaller. By comparison, the range of Al concentration is more likely to represent pre-diffusion conditions, because Al diffuses the slowest among the elements considered in our model (e.g. Spandler & O'Neill, 2010). Therefore, we use the range of measured Al concentrations to determine the pre-diffusion range of Fo (from the modelled LLD) which in turn constrains the pre-diffusion range of other elements. Within the chosen concentration range of individual elements, we sampled *n* (=number of measurements) modelled values equally distributed (see the white circles in Fig. 6a) and used them to calculate cov_{A-B}[model]. The misfit of the modelled covariance of concentrations of component pair *A*-*B* to the observation is calculated using the following equation:

$$\mathbf{Misfit}_{A-B} = \left(\frac{\mathrm{cov}_{A-B}[\ \mathbf{data}\ ] - \mathrm{cov}_{A-B}[\ \mathit{model}\ ]}{\sigma_{\mathrm{cov}_{A-B}[\ \mathit{data}\ ]}} \right)^2. \quad (4)$$

The sum of $\mathbf{Misfit}_{A-B}$ for all component pairs, i.e. Σ(Misfit), is used as an indicator of the goodness of fit. The uncertainties on the measured concentrations (referring to those determined for olivine secondary standards from this study; see Methods section) were taken in the calculation of $\sigma_{\mathrm{cov}_{A-B}[\ \mathbf{data}\ ]}$, using a Monte Carlo algorithm. This allows analytical noise to be considered in the calculation of misfits. The misfits are shown in Fig. 6 (for Hawai'i) and Supplementary Figs S12 and S13 (for Galápagos and Iceland as examples).

The fractionation models show that measurements on olivines from individual ocean islands cannot be fitted by a single LLD, implying an effect of other factor(s), such as diffusive resetting, which we assess using the approach described below.

Prediction of olivine composition modified by diffusive resetting

For diffusion modelling, we calculate element diffusivities using the Arrhenius relations determined by previous experimental studies (see review by Costa (2021) and references therein), showing the following relationship (at given temperature): $D^*_{Fe-Mg} \approx D^*_{Mn} \approx D^*_{Cr}$ **(fast)** $> D^*_{Ni} > D^*_{Cr}$ **(slow)** $> D^*_{Ca} > D^*_{P} \approx D^*_{Al}$ (diffusivity is denoted as D^* to distinguish from the partition coefficient *D*; Supplementary Fig. S11), where the D^*_{Cr} **(fast)** reported by Jollands *et al.* (2018) is an order of magnitude larger than the D^*_{Cr} **(slow)** reported by Ito & Ganguly (2006). To investigate the effect of D^*_{Cr} on the model results, we used D^*_{Cr} **(slow)** and D^*_{Cr} **(fast)** respectively for Hawaiian olivines and obtained results showing similar fits to the data. Considering this, we decided to take D^*_{Cr} **(slow)** for all ocean islands in this study for the sake of consistency. We use an intermediate pressure at crustal level (500 MPa), an oxygen fugacity at fayalite–magnetite–quartz (FMQ) buffer, and average T_{crys} calculated for the most forsteritic population at each ocean island to calculate diffusivities. The T_{crys} may be higher than the temperature when diffusion takes place (considering cooling during fractionation). However, given our interest in the diffusion-induced olivine compositional variability rather than the diffusion timescale, we regard the average T_{crys} as a realistic approximation.

An ideal model of diffusive resetting on olivine crystals in a mush pile should consider both intra-crystal diffusion (in olivine) and inter-crystal diffusion (in interstitial melts), as which of the two acts as the rate-limiting process depends on differences in diffusion distances (*x*) and diffusion rates (D^*) of given elements in the two phases (based on $x \propto \sqrt{D^* \times t}$, where *t* is diffusion time). For example, Fe–Mg diffusion in olivine is about five orders of magnitude slower than that in basalt at about 1250°C (based on second-type binary effective diffusion (SBED) of Mg in basalt; Chen & Zhang, 2008), however, the diffusion distance in olivine (limited by its grain size) can be orders of magnitude smaller than that in interstitial melts in a crystal mush. Nevertheless, since the aim of this model is investigating diffusion-induced olivine compositional variability rather than the timescale (see above), we decided to focus on diffusion modelling of olivine. More advanced models accounting for diffusion in olivine and melts can be developed in the future. Considering that all crystals in the same mush pile tend to be reset towards an intermediate composition, we fix the boundary condition of the diffusion model using the average (measured) composition of the most forsteritic population. The initial condition (at time = 0) is defined by the fractionation model. To calculate cov_{A-B} for the diffusion models, the same strategy was adopted as applied to the fractionation model, where $n = n$[**measured**] data points were sampled (with a given spacing) from the modelled concentration range to *just* cover the range of the measured Al contents (Fig. 6).

Evaluation of the effects of fractionation and diffusive resetting

For most ocean islands in this study (see an example of Hawai'i in Fig. 6), we find that the misfits of compositions predicted by the fractionation model at time = 0 (Fig. 6d) can be reduced by diffusion with time (Fig. 6e-f), and the sum of misfits reaches a minimum after given durations of diffusion (Fig. 6g). An exception exists in the case of Borgarhraun, Iceland, where the (single LLD) fractionation model produces slightly smaller covariances (cov_{A-B}[**data**]) than the observation and the diffusion models further decrease the covariances and increase the misfits to the data (Supplementary Fig. S13). This indicates a dominant controller of olivine compositions of Borgarhraun that could be different from other localities (see Discussion section). Except for Borgarhraun, our results indicate a common occurrence of diffusive resetting in forsteritic olivine from most ocean islands. This explains why 97% of the T_{crys} calculated using thermometer Equation (2) in this study (involving fast diffusing Fe–Mg) are lower than those calculated using thermometer Equation (1) (without Fe–Mg). These findings are consistent with diffusive reequilibration of olivine in mush piles previously reported for multiple ocean islands (e.g. Hawai'i; see Discussion section). In addition, we noticed that the cov_{A-B}[**data**] of most component pairs can be fitted by those generated by certain diffusion models, except for Cr-involving pairs (Fig. 6), despite using D^*_{Cr} **(fast)** or D^*_{Cr} **(slow)**. This may be due to the influence of spinel crystallisation on the melt-olivine composition that is omitted in this model and/or a relatively large uncertainty in Cr due to its low concentrations in olivine.

Overall, our modelling results indicate some extents of diffusive resetting (i.e. scenario (ii) above) in most forsteritic ocean island olivines in this study. Diffusion resetting drove the Fo contents of the high-Fo population of olivine towards an intermediate value and presumably had a larger effect on the T_{crys} calculated from Equation (2) than Equation (1) (see above). Considering this, olivine grains of intermediate Fo contents may be least affected by diffusion resetting, thus we decided to take the average Fo and

T_{crys} of the forsteritic sub-population of olivine as one endpoint of the LLD to calculate T^{prim}_{crys} (Table 1). Further work would be required to rule-in the mixing between melts derived from different lithologies (i.e. scenario (i) above) having operated as well.

Determining primary olivine Fo at the ending point of the reverse LLD

With one endpoint of the LLD determined above, we need to decide the other endpoint where the primary olivine at Fo_{prim} was produced. The value of Fo_{prim} cannot be measured directly and was usually taken as a fixed value (e.g. Fo_{91} in Matthews *et al.*, 2021) or a range (e.g. between 90 and 92; Green *et al.*, 2001; Putirka *et al.*, 2007), based on the maximum olivine Fo contents observed in natural or experimental products. With the LLD calculated from this study we find that increasing Fo_{prim} from 91 to 92 can cause an increase in T^{prim}_{crys} by 40°C to 50°C (similar to the uncertainty in T_{crys} in this study), thus it may have some effect on the calculated T_p. Here we attempted to calculate Fo_{prim} for individual ocean islands, based on liquid compositions modelled using THERMOCALC (Powell *et al.*, 1998; see detail in Supplementary Materials) and the two lithology-derived primitive liquid fractions predicted by our mantle melting model (Fig. 4).

The two melting lithologies considered in our mantle melting model (i.e. KLB-1 lherzolite and KG1 pyroxenite) were used for the THERMOCALC calculations for the sake of consistency. Liquid compositions were calculated over a wide range of *P*–*T* conditions (see Supplementary Materials, Sections 5 and 6), from which interpolation was applied to determine primitive (single lithology derived) liquid compositions at the base of the lithosphere (for OIs; Fig. 4b) with given liquid fractions that are unknown (see the two lithology-derived liquid compositions and the python codes we used in a Zenodo repository; Li, 2025). To determine the primitive liquid composition, we use the single lithology derived liquid fraction (F_{px}, F_{lz}) predicted by the mantle melting model with given T_p–φ_{px}–φ_{hz}, and then mix the two liquids following the proportions (X_{px}, X_{lz}) predicted with the same T_p–φ_{px}–φ_{hz} (Fig. 4). The predicted primitive liquid has known ferrous Fe (calculated as $Fe^{2+} = FeO_t - 2*O$) and Mg concentrations which were used to calculate Fo_{prim}, taking $Kd^{ol-liq}_{Fe^{2+}-Mg}$=0.3 ±0.03 (Roeder & Emslie, 1970). With the above-mentioned method, we obtain Fo_{prim} between 92.1 and 95.3 (Table 2), higher than the highest OIB olivine Fo of 80 to 92.3 compiled in GEOROC database (Fig. S2). Calculations using such high Fo_{prim} produce very high T_p up to 1891°C (median: 1643°C; see Table 2). If we take a higher *Kd* of 0.34 (e.g. Matzen *et al.*, 2011; Putirka 2016; see Discussion section), the Fo_{prim} will be reduced by less than one unit (=91.1–94.7) and be more similar to the observations but still higher than most. The Fo_{prim} calculated with this approach is likely to be systematically overestimated and produce incorrect estimates of T_p (Table 2). Therefore, we decide to conservatively take Fo_{prim}=91 to calculate T^{prim}_{crys} for all ocean islands and mid-ocean ridge from this study (Table 1) and use these values to invert T_p.

AN INVERSION ROUTINE FOR MANTLE POTENTIAL TEMPERATURE

The input parameters of the adiabat mantle melting model we use are T_p, φ_{px} and φ_{hz}. Parameter values were chosen from predefined probability distributions, i.e. T_p between 1300–2000°C, and φ_{px} and φ_{hz} between 0–1, for forward modelling that generates T^{prim}_{crys}. The misfit of the forward modelled T^{prim}_{crys} to that calculated from projecting the high-Fo olivine back to Fo_{prim}=91 was evaluated with a log-likelihood function, which refines the parameter values to be used by the subsequent forward models. The process is repeated until the maximum likelihood region is sufficiently characterised to estimate the posterior probability distribution of T_p, φ_{px} and φ_{hz}. A Bayesian Monte Carlo inversion routine was used following Matthews *et al.* (2021), to find the parameter values producing T^{prim}_{crys} in the best match with the observation.

Compared to the T^{prim}_{crys} inverted to estimate T_p for ocean islands, additional parameters are available for mid-ocean ridges (in this work Siqueiros, and Iceland at its coasts). These include the crustal thickness (t_{crust}) that constrains the total melt fraction *F* (Fig. 4), and the contribution of pyroxenite-derived melts to the volume of the crust (X_{px}*, denoted with an asterisk as it may involve different flow regimes from ocean islands; e.g. Ito & Mahoney, 2005a, 2005b), which was estimated from magma chemistry and constrains the melt fraction of the pyroxenite (F_{px}; see the X_{px}*–F_{px} relationship in Equation (5) of Matthews *et al.*, 2021). Here we adopt the values of t_{crust} and X_{px}* from Matthews *et al.* (2021), i.e. t_{crust} = 5.74 (±0.27) km and 20 (±1) km, and X_{px}* = 0.175 (±0.1) and 0.3 (±0.1) for Siqueiros and Iceland, respectively. The additional constraints produce smaller uncertainties in the T_p calculated for the mid ocean ridges (12–15°C) than the ocean islands (>30°C) in this study (Table 2).

MODEL RESULTS

We applied the approaches described above to 17 ocean islands (including those in Table 1 and Rurutu, Austral in Supplementary Tables S1 and S5) and Siqueiros. The olivine–spinel pairs used to calculate T_{crys} were obtained for 15 islands in this study, and taken from previous studies on two other localities, i.e. Kama'ehuakanaloa (previously known as Lō'ihi), Hawai'i (Matthews *et al.*, 2021) and Borgarhraun, Iceland (Matthews *et al.*, 2016), and Siqueiros (Coogan *et al.*, 2014; Matthews *et al.*, 2021). Preferred values of T_{crys} were taken from either thermometer Equation (1) or (2) based on the statistical test described above. The average T_{crys} and Fo of the most forsteritic sub-populations of olivine are used to calculate T^{prim}_{crys} (considering the effect of diffusive resetting) (Tables 1-2). The selected olivines are representative of the most forsteritic populations at individual ocean islands (the observed maximum Fo contents are either higher or close to those previously reported and compiled on the GEOROC database; Supplementary Fig. S2). Results calculated using Fo_{prim}=91 or variable Fo_{prim} are summarised in Table 2. To investigate the effect of the pre-defined range of T_p on the results, we carried out the same calculations using a wider range (1300–2000°C) and a narrower range (1300–1675°C); the upper limit of 1675°C was estimated using the method in this study to be the threshold temperature of a pure lherzolitic mantle melting at 10 GPa. Median T_p calculated from the two input T ranges show small differences (−9 to 53°C) considering uncertainties in these values (±18 to ±115°C; Table 2). Therefore, we focus on the results calculated using Fo_{prim}=91 and an input range of 1300°C to 2000°C hereafter. We notice that using T^{prim}_{crys}=1477°C and 1454°C (calculated from two different LLD methods; see above and Supplementary Table S6) to calculate T_p for Austral produce very different results, i.e. the former providing no solution whereas the latter yielding a high median with a large uncertainty (1620 ± 102°C). These imply that the calculations for Austral (e.g. with a high T^{prim}_{crys} of 1477°C and a thin lithosphere of ~47 km) may be pushing the limit of the method we use (see Discussion

Table 2: The median and 1σ of T_p (°C) calculated using fixed or variable primary olivine forsterite contents

Location	primFo = 91					variable primFo				Excess T
	T_{crys}^{prim}†	T_p	1σ	T_p*	1σ	primFo	1σ	T_p	1σ	
Azores	1280	1368	48	1357	41	93.5	1.3	1674	196	18
Balleny	1431	1573	99	1562	74	92.8	1.0	1749	151	223
Cape Verde	1332	1393	31	1396	31	94.5	1.1	1763	87	43
Crozet	1273	1327	18	1328	20	95.3	0.3	1891	49	−23
Fernando de Noronha	1442	1579	71	1558	60	92.1	1.1	1586	104	229
Galápagos	1364	1484	52	1486	58	92.9	0.8	1597	73	134
Gough	1450	1613	73	1592	53	92.9	0.9	1605	82	263
Hawai'i	1394	1515	66	1516	58	92.1	1.1	1587	100	165
Juan Fernandez	1376	1511	74	1511	72	92.9	0.9	1597	92	161
Réunion	1410	1552	54	1542	52	92.4	1.1	1588	89	202
Marquesas	1383	1491	52	1500	51	92.2	0.9	1586	89	141
Society	1363	1448	53	1448	55	92.9	2.1	1695	167	98
St. Helena	1482	1661	108	1608	47	92.8	0.9	1603	72	311
Trindade	1343	1419	40	1416	38	93.8	1.6	1681	143	69
Tristan da Cunha	1454	1625	91	1587	55	93.3	0.7	1610	66	275
Average		**1504**		**1494**		**93.1**		**1654**		**154**
Siqueiros MOR	1226	1350	12	1350	12	92.1	0.5	1464	31	0
Iceland	1363	1530	15	1530	15	93.4	0.5	1576	27	180

†Uncertainties in T_{crys}^{prim} were taken from those in the mean T_{crys} in Table 1. *The range of input T_p was set as 1300–1675°C for these model runs to be compared with the other two groups of results in this table that used input T_p between 1300–2000°C (see main text).

section) and produce T_p of large uncertainties. Therefore, we exclude Austral from the comparison with other ocean islands hereafter.

Median T_p were estimated as between 1327 ± 18°C (Crozet) and 1661 ± 108°C (St. Helena), with an average value of 1504°C across all ocean islands (Table 2; see posterior distributions in Supplementary Figs S21–S35). Median values of lithology fractions are φ_{px} = 0.07–0.19 and φ_{hz} = 0.47–0.69, and the 68% confidence interval of most ocean islands overlap with each other (Fig. 8 d-e; see values in Table S7). Iceland has similar median T_p (1530 ± 15°C) and φ_{px} (0.08 ± 0.03) to other ocean islands, although with much lower φ_{hz} (median: 0.27 ± 0.11). In comparison, the potential temperature, pyroxenite fraction, and harzburgite fraction are all lower for the Siqueiros MORB, i.e. T_p = 1350 ± 12°C, φ_{px}=0.03 ± 0.01, φ_{hz}=0.23 ± 0.16 (Fig. 8 d-e) (Table S7). Taking the T_p of Siqueiros as an approximation of the average value for mid-ocean ridges (i.e. T_p^{MOR}=1350 ± 12°C), we obtain plume excess temperatures $\Delta T_p = T_p^{OI} - T_p^{MOR}$ of −23°C (Crozet) to 311°C (St. Helena), with uncertainties of ±22 to ±116°C considering the uncertainty in T_p^{OI} and T_p^{MOR}.

The posterior distributions were also investigated for their co-variation (Supplementary Fig. S54). The median T_p[[ineq199]]is positively correlated with T_{crys}^{prim}(correlation coefficient R: 0.98; Fig. 8a) and median φ_{px} (R: 0.98; Fig. 8d) and inversely correlated with median φ_{hz} (R: −0.87; Fig. 8e). The median φ_{hz} decreases with increasing φ_{px} and stabilises at $\varphi_{hz} \approx 0.49$ when $\varphi_{px} > 0.13$ (Supplementary Fig. S53). Similar relationships were pointed out by Matthews *et al.* (2021) and emerge because of these two lithologies' contrasting effects on the thermal structure of the melting region (see detail in Discussion section). Nevertheless, when the proportion of pyroxenite is sufficiently high in the mantle source, the presence of harzburgite is required to ensure buoyancy of the plume, even if the plume temperature is high.

Of potential concern is the strong inverse correlation between T_p and the maximum observed Fo (Fo_{max}^{obs}) (R: −0.84; Fig. 8b). This could be a real property of these systems, indicating that plumes with the highest temperature either have sources producing more iron-rich olivines (i.e. pyroxenite-rich), or create overlying magmatic plumbing systems more prone to erupting evolved magmas. Alternatively, we could be seeing an artefact of the inverse extrapolation of LLD applied to calculate T_{crys}^{prim}. For locations where the maximum observed Fo is low (e.g. ≤ 85), the melt may have crystallised minerals other than olivine, which would lead to a shallower gradient in Fo–T_{crys} space, therefore, the T_{crys}^{prim} (hence T_p) could be overestimated. We investigated the effect of clinopyroxene crystallisation on T_{crys}^{prim} using the same THERMOCALC model as mentioned above and Petrolog3 (Danyushevsky & Plechov, 2011). The two models provided similar results: calculation using THERMOCALC indicates that having 5% clinopyroxene coexisting with olivine and a KG1-derived or KLB1-derived melt could cause a ~20°C or ~40°C overestimate of T_{crys}^{prim}, whereas fractionation modelling of a pure KG1-derived melt using Petrolog3 indicates that 3% clinopyroxene co-existing with olivine could cause an overestimation of ~11°C. Evidence for possible concurrent crystallisation of clinopyroxene-olivine was observed in low-Fo olivines from a few ocean islands, showing a drop of Ca with decreasing Fo content at Fo < 85 (see Discussion section).

For this set of results, the input lithospheric thickness (45–95 km) does not show any strong correlation with the posterior parameters (R < 0.5; Fig. 8f). The effect of lithospheric thickness on the inverted T_p and source lithology fractions in this study was found to be rather small (see Discussion section).

DISCUSSION

Effects of fractional crystallisation, diffusive resetting, and magma mixing on olivine composition and temperature estimation

For most ocean islands investigated in this study we find that the measured olivine compositions cannot be fitted by pure fractional crystallisation. Instead, the elemental covariances require diffusive resetting to have occurred (see above). Modelling the diffusive relaxation of the olivine populations, we obtained particularly good fits for olivine chemistry from Kama'ehuakanaloa, Hawai'i (Fig. 6) and Galápagos (Supplementary Fig. S12). This

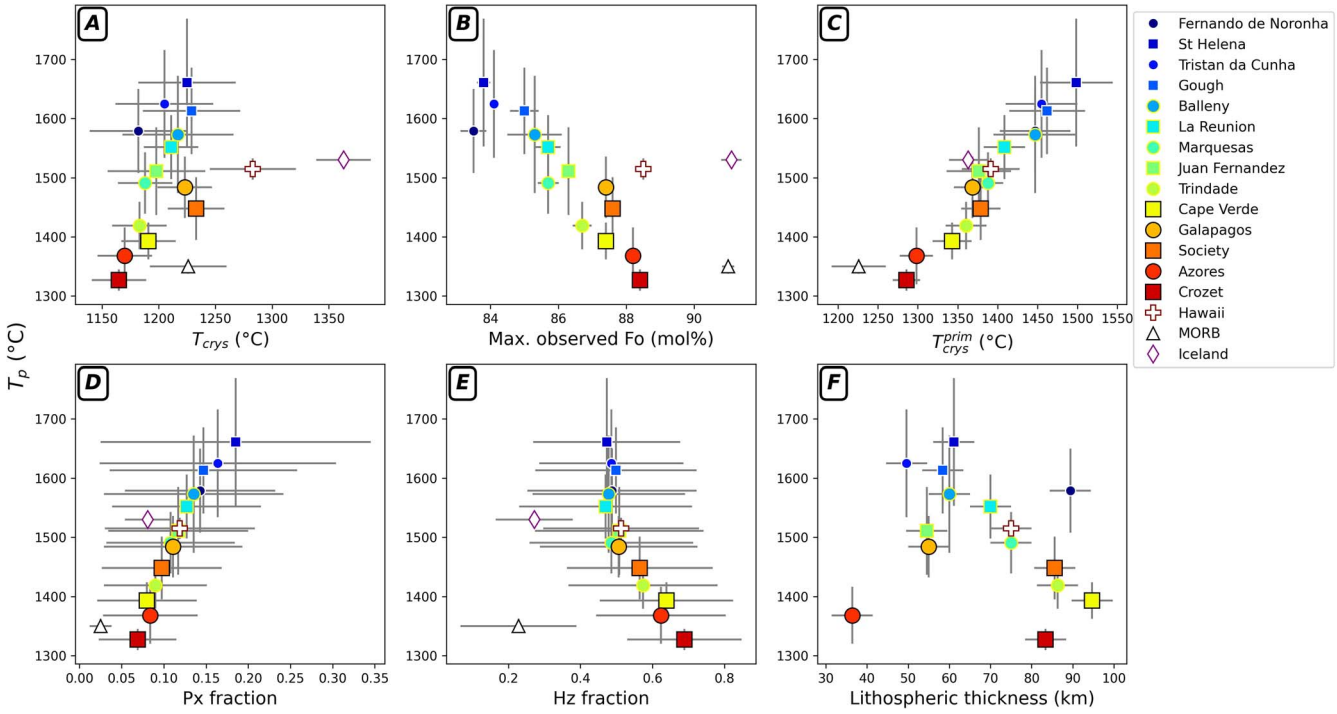

Fig. 8. Estimates of T_p using a fixed primary olivine Fo_{91}, plotted versus (*a-b*) crystallisation temperature and Fo contents of the most forsteritic olivines found for individual ocean island in this study, (*c*) the calculated primary olivine crystallisation temperature, (*d-e*) source lithology fractions ('Px' = pyroxenite, 'Hz' = harzburgite), and (*f*) lithospheric thickness. Results for ocean islands having different maximum Fo contents are marked in symbols with outlines in different colours for comparison (dark: Fo > 87; coloured: Fo between 85–87; white: Fo < 85).

is in coincidence with the inferred magma residence times of years to decades in these two regions (e.g. at major Hawaiian volcanoes, Lynn *et al.*, 2017; at the eastern Galápagos islands, Gleeson & Gibson, 2019), allowing the equilibration of cumulate crystal piles to occur. For the Borgarhraun olivine, we observe a different phenomenon, where the single-LLD fractionation model produced lower covariances than the data and the diffusion models produced worse fits than the fractionation model (see Supplementary Materials). Previous studies reported rather long residence times required to produce the chemical zoning observed in the Borgarhraun olivine–spinels (on the order of 1000 years; Thomson & Maclennan, 2013; Mutch *et al.*, 2019; Maclennan, 2019). Combining these findings with our model results, we suggest that diffusive reequilibration that tends to homogenise the compositions of the Borgarhraun olivine was overwhelmed by a compositional heterogeneity of the magma, possibly induced by mixing between compositionally different melts derived from different source lithologies (e.g. Maclennan *et al.*, 2003; Maclennan, 2008; Winpenny & Maclennan, 2011). This agrees with the better fits to the olivine Fo-Ni data by multiple LLDs than a single LLD observed for Borgarhraun (see Supplementary Fig. S14).

Compared to fractional crystallisation of olivine and diffusion, it is more difficult to quantitatively evaluate the effect of primary magma mixing and of co-saturation of mineral phases other than olivine on the observed olivine compositions. For the co-saturation of clinopyroxene and plagioclase, one may investigate it by modelling the fractional crystallisation of a primary liquid (using existing thermodynamic models). However, the primary liquid composition is usually unknown, and deriving it from the liquid in equilibrium with the available olivine is problematic, as one would not know when to stop the liquid being multiply saturated. Therefore, here we empirically investigate the effect of mixing and co-saturation based on the analysed olivine composition. Co-saturation of plagioclase/clinopyroxene and olivine should produce a noticeable shift in the Fo–Ca relationship of olivines, whereas mixing of compositional heterogeneous primitive magmas should produce a larger variation in olivine Mn contents (with Mn being incompatible in most minerals) than without mixing. Our findings are as follows.

We find that the most forsteritic populations of olivine generally follow the Fo–Ca variation predicted by olivine-only LLDs (Supplementary Fig. S10), but the less forsteritic olivine (Fo_{85}) commonly show Ca concentrations lower than prediction of LLDs, possibly indicating clinopyroxene crystallisation. At some ocean islands (e.g. Azores, Galápagos,Hawai'i, Marquesas), this is supported by olivine Ni contents higher than those predicted by the LLDs (Supplementary Figs S8 and S9). Although it is difficult to precisely determine the Fo at clinopyroxene-in due to gaps in Fo contents of the available data in this study, our observation of olivine Fo < 85 at clinopyroxene-in agrees with previous findings using fractional crystallisation models (e.g. Fo ≈ 83 for eastern Galápagos islands; Gleeson & Gibson, 2019) and observations based on more continuous arrays of olivine data (e.g. Fo ≈ 84.5 for St. Helena; Kawabata *et al.*, 2011).

For Mn, we find that the concentrations in the most forsteritic populations of olivine are well fitted by single LLDs for most ocean islands in this study. An exception is observed from Fernando de Noronha where the most forsteritic olivine we analysed have low Fo contents (≤84) and show larger Mn–Fo gradients than those predicted by a single LLD; a similar trend is seen in Ca, but not in Ni or Al (Supplementary Figs S6–S10). Given the identical diffusion rates of Mn and Fe–Mg but much slower diffusion rate of Ca, the observed trends cannot be explained by single LLDs plus diffusive resetting (Supplementary Fig. S14). They may be caused by some extent of mixing towards a more evolved melt that is not

considered in our model or be biased due to a restricted number of crystals available. Nevertheless, since the Al concentrations and T_{crys} of Fernando de Noronha and the other ocean islands from this study match well with those predicted by single LLDs, our choice of taking the average T_{crys} to calculate T_{crys}^{prim} is sensible (Fig. 5), despite that the possibility of melt–melt mixing cannot be ruled out.

Overall, this discussion highlights the importance of knowing the wider petrological context in attempting to reconstruct T_p from olivine-based thermometry, as some of this information is difficult to know from the olivine crystals in isolation.

Uncertainties in the primary olivine Fo and crystallisation temperature

We calculated T_p using either a primary olivine Fo content ($\mathbf{Fo}_{prim}$) of a constant value (=91), or variable values predicted by the forward model of multi-lithology melting itself (see approaches in Supplementary Materials). In both scenarios, we find that the T_p estimate is dominantly controlled by T_{crys}^{prim} and the two show a positive correlation (see Fig. 8a and Supplementary Fig. S20), in agreement with findings of previous studies (e.g. Herzberg & Asimow, 2015; Herzberg *et al.*, 2023). Uncertainties in the T_{crys}^{prim} and[[ineq220]]T_p calculated under the two scenarios are discussed below.

When $\mathbf{Fo}_{prim}$ is fixed, we find a negative correlation between T_{crys}^{prim} and the maximum olivine Fo ($\mathbf{Fo}_{max}^{obs}$) observed from given localities: the second lowest $\mathbf{Fo}_{max}^{obs}$ of 83.8 at St. Helena yields the highest T_{crys}^{prim} of ~ 1499°C (using the modelled reverse LLD) and the highest T_p of ~ 1661°C. This may be attributed to possibly larger extents of overestimation on T_{crys}^{prim} (hence T_p) due to larger errors induced by reverse fractionation modelling over large Fo intervals (e.g. from Fo85 to Fo91). The main source of errors in the calculation of T_{crys}^{prim} include: (i) variations in input parameters (e.g. melt alkali content) during olivine fractionation, (ii) the selection of equations applied to calculate olivine saturation temperature (e.g. those of Putirka *et al.* (2007) used in this study versus other studies; e.g. Herzberg & Asimow, 2008), and (iii) possible co-saturation of low-Fo olivine and other minerals generating smaller olivine Fo-temperature gradients than predicted by an olivine-only LLD (see above). This is also evident when comparing the estimates of excess temperatures from this study and previous geophysical studies (see the following subsection), where a high T_{crys}^{prim} was estimated for a locality above a thin lithosphere (e.g. Austral), a very high mantle temperature exceeding the solidi of the source lithologies at depths (e.g. 10 GPa) will be produced leading to estimates of T_p that may greatly deviate from the true value, thus Austral was excluded from this study.

When a variable $\mathbf{Fo}_{prim}$ is used to calculate T_{crys}^{prim}, the uncertainty in the estimated mantle temperature increases significantly (see Supplementary Fig. S20). As for the approach used in this study, errors mainly arise from two aspects: (1) primitive liquid compositions derived from THERMOCALC modelling, and (2) $Kd_{Fe^{2+}-Mg}^{ol-liq}$=0.3, which we discuss below.

For aspect (1), there is an inherent, and hard to quantify, error in any model's prediction of primary liquid compositions, induced by uncertainties in the experimentally informed thermodynamic database and liquid-mineral models. An indication of the error that may emerge here is to compare between two thermodynamic models (e.g. as done by Stolper *et al.*, 2020). However, few models are available for pyroxenite melting.

For aspect (2), many experimental studies have determined $Kd_{Fe^{2+}-Mg}^{ol-liq}$ and reported different values and formulas. Roeder & Emslie (1970) proposed $Kd_{Fe^{2+}-Mg}^{ol-liq}=0.3\pm0.03$ (assuming all Fe as Fe^{2+}, adopted by many previous studies and this study). Toplis (2005) proposed an equation applicable to a wide compositional range of mafic-felsic melts, based on temperature, pressure, olivine Fo content, and molar silica content of the liquid. Blundy *et al.* (2020) proposed an equation for basaltic and basaltic andesitic melts based on Fo content and recognised the role of liquid $Fe^{3+}/\sum Fe$ in setting the olivine–melt Fe exchange. An inherent challenge in employing any such equation in the present study is that the liquid composition in equilibrium with the olivine of interest needs to be known, however, the primitive crystals that are useful for mantle temperature reconstruction are often carried by more evolved liquids, while the compositions of primary liquids in equilibrium with these crystals are often unknown. Here we investigate the range of $Kd_{Fe^{2+}-Mg}^{ol-liq}$ in OIB samples in this study in three ways as described below.

First, we use the equation (8) for $Kd_{Fe^{T}-Mg}^{ol-liq}$ and equation (4) for the relationship between $Kd_{Fe^{T}-Mg}^{ol-liq}$ and $Kd_{Fe^{2+}-Mg}^{ol-liq}$ of Blundy *et al.* (2020) to write the following equation: $Kd_{Fe^{2+}-Mg}^{ol-liq} = 0.3642 \times \exp\left[\frac{312.7(1-2X_{Fo})}{T}\right]$ (X_{Fo} is the molar fraction of forsterite in olivine; T is temperature in Kelvin). This equation accounts for non-ideal mixing in olivine solution by including Fo as a variable. Taking Fo contents of the most forsteritic population of olivine at individual ocean islands from this study, we obtain $Kd_{Fe^{2+}-Mg}^{ol-liq}$=0.307–0.316, within the presumed range (0.3 ± 0.03) (Supplementary Fig. S19). Secondly, we consider the $Kd_{Fe^{2+}-Mg}^{ol-liq}$ determined by previous partial melting experiments on the KR4003 lherzolite (Walter, 1998) and the KG1 pyroxenite (Kogiso *et al.*, 2004). We notice that these experiments produce generally higher $Kd_{Fe^{2+}-Mg}^{ol-liq}$ (KR4003: 0.31–0.36; KG1: 0.27–0.38), while their temperature (1300–1700°C) are also higher than olivine crystallisation temperatures in this study (mostly <1300°C) (Supplementary Fig. S19). Lastly, we used the compositions calculated using THERMOCALC for the primitive liquids and olivine at the top of the melting regions (pressure: 1.25–2.65 GPa) to calculate $Kd_{Fe^{2+}-Mg}^{ol-liq}$, and obtain values also within the presumed range of 0.3 ± 0.03, i.e. 0.29 to 0.33 (median: 0.30) for lherzolite-derived liquids, and 0.28–0.30 (median: 0.29) for pyroxenite-derived liquids (Supplementary Fig. S19).

Overall, most values derived from the three methods above overlap with 0.3 ± 0.03, implying that taking $Kd_{Fe^{2+}-Mg}^{ol-liq}=0.3\pm0.03$ is a reasonable approximation under most conditions concerned in this study. Nevertheless, it is worth noting that the primitive liquids calculated from THERMOCALC have rather high Mg#, using which and $Kd_{Fe^{2+}-Mg}^{ol-liq}$=0.3 yielded an overestimation on $\mathbf{Fo}_{prim}$ (~92–95) for ocean islands in this study. By comparison, better model fits for T_{crys}^{prim} were acquired using the more plausible $\mathbf{Fo}_{prim}$= 91 (Supplementary Figs S21–S35).

The discussion above indicates that any decision about reconstructing primary liquids requires compromise and introduces its own sources of uncertainty. Using a fixed value for $\mathbf{Fo}_{prim}$ to calculate T_{crys}^{prim} and mantle temperature yields plausible results but is potentially inconsistent with inferences about the source lithology, which might suggest lower Fo in the source regions of some localities discussed here. Using variable $\mathbf{Fo}_{prim}$ increases consistency but introduces the poorly constrained errors of complex thermodynamic models of mantle melting. Considering this, we have more confidence in the fixed $\mathbf{Fo}_{prim}$ results. Further investigation of the $\mathbf{Fo}_{prim}$ variability at different localities would be necessary for reducing uncertainties on the mantle temperature estimates.

Trade-offs between mantle temperature and source lithology

Mantle plumes are frequently described as comprising at least two different lithologies: peridotite, which explains key features of mantle structure (e.g. Ringwood, 1962; Green & Ringwood, 1967), and recycled oceanic crust (e.g. Stracke *et al.*, 2003; Sobolev *et al.*, 2007), the amount of which differs between locations. More recently, emphasis has been placed on the possible presence of an additional lithology—refractory harzburgite—in mantle plumes (e.g. Kelemen *et al.*, 1992; Nakagawa *et al.*, 2010; Shorttle *et al.*, 2014; Matthews *et al.*, 2016). Melting of the different lithologies mentioned above extract distinct amounts of latent heat (e.g. Matthews *et al.*, 2016), which, on top of variations in plume temperatures, causes variations in the primitive crystallisation temperature that may be preserved in/extracted from volcanic samples. Accounting for a lithologically heterogeneous mantle is, therefore, critical for accurately estimating its temperature. However, including lithological heterogeneity in such a model potentially opens a very wide parameter space, as the composition and melting behaviour of recycled materials can vary widely (e.g. Lambart *et al.*, 2016). This is not a challenge we address in this study as we focus instead on modelling three lithologies and propagating the uncertainty that introduces on its own into mantle temperature estimation.

With a multi-lithology mantle melting model such as that used in this study and by Matthews *et al.* (2021), the uncertainty on the proportions of individual lithologies in the mantle source can be great. As demonstrated in Fig. 9, (fictive) pure lherzolite, harzburgite, and pyroxenite mantles can produce the same primary liquid temperature on top of the melting region, but with widely different T_p, the values of which required for the lherzolite-only and harzburgite-only mantle are almost identical (since the degree of lherzolite melting is small), whereas that required for the pyroxenite-only mantle is about 250°C to 350°C higher (the thinner the lithosphere, the larger the difference). In other words, when fitting a single value of $T_{\mathrm{crys}}^{\mathrm{prim}}$ (derived from the olivine observed) using a multi-lithology mantle melting model, there may be multiple solutions for mantle T_p and source lithology fractions. Even though a constraint of positive plume buoyancy was applied in this study, the permissible parameter space could be large.

Previous studies investigated the interplay between T_p, lithospheric thickness and the amount of recycled crust (e.g. Sobolev *et al.*, 2007) and found that a thin lithosphere (e.g. MORB, Iceland and Azores) favours a high proportion of peridotite-derived melt, whereas a thick lithosphere (e.g. LIPs) favours a high proportion of pyroxenite-derived melt (X_{px}, equal to the proportion of lherzolite-derived melt (X_{lz}) subtracted from 100%). This is supported by results for a few ocean islands in this study, showing higher X_{px} with thicker lithosphere (Supplementary Fig. S52). Specifically, the median X_{px} calculated for ocean islands with lithospheric thickness of 35 to 75 km (e.g. 0.41 ± 0.28 to 0.64 ± 0.30 in Azores, Galápagos, Hawai'i, and Réunion) are lower than localities with thicker lithosphere (83–95 km for Crozet, Trindade and Cape Verde, where median $X_{px} \approx 1$). The positive correlation between X_{px} and lithospheric thickness is stronger for islands providing high-Fo olivines than those providing low-Fo olivines, consistent with the more accurate estimates of mantle temperatures and lithology fractions derived from forsteritic olivines as discussed above. One exception is Azores (Flores), which has a thin lithosphere beneath the island where samples in the study were collected (~36 km) but provided a rather high median X_{px} (0.60 ± 0.24). This may be related to the more complex magmatism at the Azores archipelagos as it is located near the Mid-Atlantic Ridge. The Flores Island, where samples in this study are from, is the westernmost island of Azores, and its volcanic activities (dated back to ~2.1 Ma) may have started earlier than most other islands of the archipelagos (i.e. younger than 1.3 Ma) (Zanon, 2015). Previous studies have shown that some olivine-hosted melt inclusions from Flores were extremely depleted (with high Nd isotope signatures) compared to those from two other islands (Pico and Corvo) of Azores, indicating a heterogenous mantle and high proportion of melt contribution by ultra-depleted mantle (Stracke *et al.*, 2019). Considering this, the fraction of pyroxenite-derived melt at Azores may be lower than the estimate in this study, which would correspond to a lower T_p hence lower excess temperature.

Furthermore, we investigated the effect of lithospheric thickness by running the mantle melting model for Azores using a higher lithospheric thickness (~45 km, at Pico Island; Dasgupta *et al.*, 2010) and the same values for the other parameters. Compared to our results for Flores Island (lithospheric thickness of ~36 km), the calculation with a thicker lithosphere yielded similar median values of source lithology fractions ($\varphi_{px} \approx 0.08 \pm 0.06$, and $\varphi_{hz} \approx 0.62 \pm 0.18$) but 15°C lower T_p (still within each other's uncertainty, i.e. 1368 ± 48°C versus 1353 ± 42°C). The different T_p but same primary magmatic temperature can be explained by a larger amount of heat consumed during melting beneath a thinner lithosphere (i.e. melting ceases at a shallower depth). This indicates that lithospheric thickness is not the major source of errors on the T_p calculated using methods in this study. Considering the thin lithosphere beneath Flores and possible overestimation of pyroxenite-derived melt (see above), the excess temperature reported for Azores in this study likely represents the maximum.

In addition, we compare the multi-lithology model results from this study with those calculated using PRIMELT3 (Herzberg *et al.*, 2023) which focuses on peridotite melting and calculates olivine crystallisation temperatures using liquid compositions. Our estimates of T_p mostly overlap with results reported by Herzberg *et al.* (2023) for Siqueiros (1365 ± 14°C), Hawai'i (Mount Kea: 1520–1560°C), and Iceland (Western Volcanic Zone: 1340–1520°C). We note that the comparable results were yielded by greatly different approaches applied in this study and by Herzberg *et al.* (2023), i.e. using T_{crys} calculated from olivine–spinel composition versus liquid MgO content, and modelling melting of a multi-lithology versus single-lithology mantle. We suspect that this could be due to the trade-offs between mantle temperature and source lithologies discussed in this section. For localities with good constraints on the source lithology fractions, such as Iceland, we found a small range of T_p ($=1530 \pm 15$°C) with a median value higher than that of Herzberg *et al.* (2023). The higher T_p estimates could be due to pyroxenite melting considered in our model but not in PRIMELT3 (focusing on peridotite sources), supported by a majority (~70%) of unsuccessful solutions provided by PRIMELT3. The temperature range we report could be smaller than the real range because we focus on the high-Fo sub-populations of olivine in this study. While our results do not exclude the possibility of thermal heterogeneity in the mantle plume below Iceland (e.g. Herzberg *et al.*, 2023) or elsewhere, it is emphasised in this study that the trade-offs between temperature and lithology fractions of source mantle can jointly produce the observed temperature variability.

The key implication from the above discussion is that having additional constraints on the mantle source lithology fractions would improve the accuracy of the T_p estimates. This is especially true for pyroxenite since its thermal effect on the melting region is so great that the inferred T_p and harzburgite-lherzolite fractions

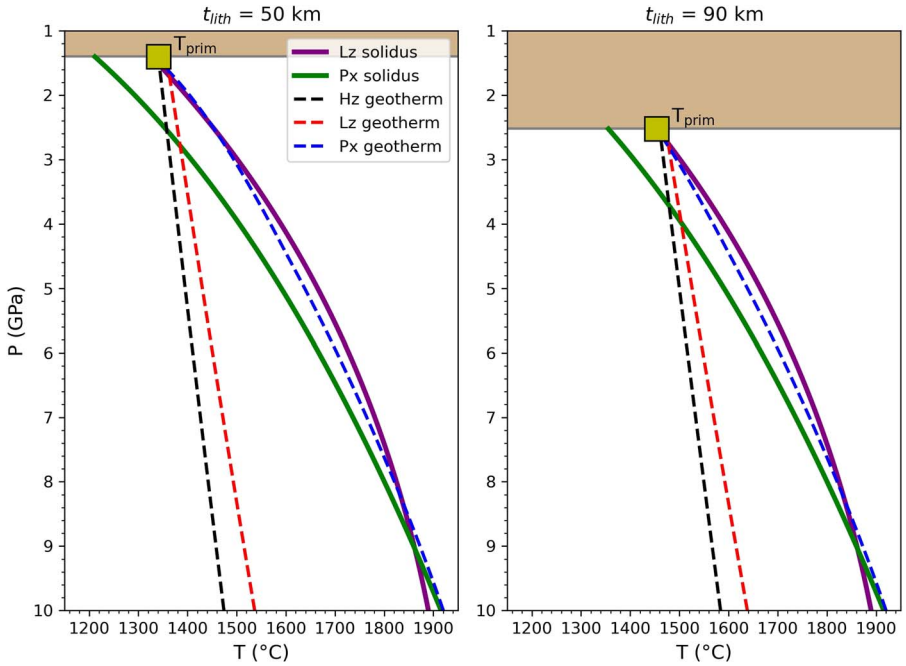

Fig. 9. Geotherms calculated for fictive single-lithology mantle sources that yield the same primitive melt crystallisation temperature at the top of the melting region (lithosphere marked in coloured areas), but with dramatically different temperatures at 10 GPa (dashed lines in different colours represent geotherms derived from different source lithologies). Note that the requirement for source buoyancy is not considered in these illustrative scenarios.

vary significantly to compensate (Fig. 9). Better constraints on these may be inferred in the future by broader inversion of crystallisation temperature estimates alongside further constraints on primitive magma chemistry (e.g. based on REEs; Wong *et al.*, 2022) and seismic velocity structures (e.g. Bao *et al.*, 2022) at these ocean islands.

Comparison with excess temperatures from the literature

We used the T_p[[ineq259]] calculated using $\mathbf{Fo}_{\mathbf{prim}}$= 91 for ocean islands ($T_p^{OI}$) and a T_p^{MOR} = 1350°C for mid-ocean ridge to calculate the excess temperature ΔT_p. These results are compared with values reported by previous studies considering a single-lithology source mantle, i.e. those using an olivine–liquid thermometer and a peridotite melting model by Putirka (2008a) (T_p^{MOR} = 1396°C calculated for Siqueiros; Fig. 10a), and those using inversion of seismic velocities from the global shear wave tomography model SEMUCB-WM1 over a wide range of depths (260–600 km) by Bao *et al.* (2022) (T_p^{MOR} = 1377°C, for a depleted MORB mantle; Fig. 10b). Out of the ocean islands investigated in this study, 13 and 14 were studied by Putirka (2008a) and Bao *et al.* (2022), respectively. Here we consider that ocean islands providing olivines with Fo > 85 in this study yielded reliable estimates of T_p (see previous subsections). Comparison of these results with the two previous studies is as follows.

For the 12 ocean islands with $\mathbf{Fo}_{max}^{obs}$ >85, our estimates on ΔT_p (−23°C to 202°C) mostly overlap with those reported by Bao *et al.* (2022) (36–257°C) but show a larger difference from those reported by Putirka (2008a) (114–290°C). The best match of ΔT_p between this study and the two previous studies are found for Iceland (between 180°C and 221°C) and Galápagos (between 130°C and 185°C). To assess the causes of the difference in ΔT_p between different studies, we compare the controlling factors of (a) T_{crys}^{prim}, and (b) T_p separately as follows. Comparison of T_{crys}^{prim} calculated petrologically from Putirka (2008a) and this study shows that values reported by Putirka (2008a) (calculated using olivine–liquid thermometry of Putirka *et al.* (2007) assuming $\mathbf{Fo}_{\mathbf{prim}}$=91.5) are about 24 to 240°C higher than our results (calculated using olivine–spinel thermometry and$\mathbf{Fo}_{\mathbf{prim}}$=91). One cause of the difference is the different thermometer equations used to calculate crystallisation temperatures. Taking Siqueiros as example, a half-a-unit increase in $\mathbf{Fo}_{\mathbf{prim}}$ can increase T_{crys}^{prim} by ∼20–30°C, but the T_{crys}^{prim} reported by Putirka (2008a) is ∼130°C higher than our estimation (i.e. 1355 versus 1226°C). The T_{crys}^{prim} values reported for ocean islands by Putirka (2008a) are generally higher too. To eliminate the effect of T_{crys}^{prim} (e.g. determined by the choice of $\mathbf{Fo}_{\mathbf{prim}}$and thermometer equations as mentioned above) on ΔT_p, we defined a parameter ΔT_{crys}^{prim} (=T_{crys}^{prim} [OI] − T_{crys}^{prim} [MOR]) and compared its values together with ΔT_p between Putirka (2008a) and this study. We find that although Putirka (2008a) reported generally higher ΔT_p (by a median of ∼64°C), the ΔT_{crys}^{prim} of Putirka (2008a) and this study are less different (median difference of only ∼9°C). This indicates another cause of the difference in ΔT_p being the different mantle melting models applied. We note that the mantle melting models of Putirka (2008a) and this study exploit different thermodynamic properties of different source lithologies. Specifically, the single-lithology peridotite melting model of Putirka (2008a) is likely to predict a larger amount of heat consumption throughout the melting region, compared to the multi-lithological (lherzolite, pyroxenite, harzburgite) melting model used in this study. This would be consistent with the non-melting harzburgite having a thermal buffering effect in the melting region.

For the three ocean islands with $\mathbf{Fo}_{max}^{obs}$ <85, i.e. Fernando de Noronha, St. Helena and Tristan da Cunha, we obtained on average higher ΔT_p than Putirka (2008a) and Bao *et al.* (2022). It is noticeable that our estimation of ΔT_{crys}^{prim} are also higher than those from Putirka (2008a), which should not be affected by differences in the mantle melting models applied in different studies but are determined by the fractionation models. These are consistent

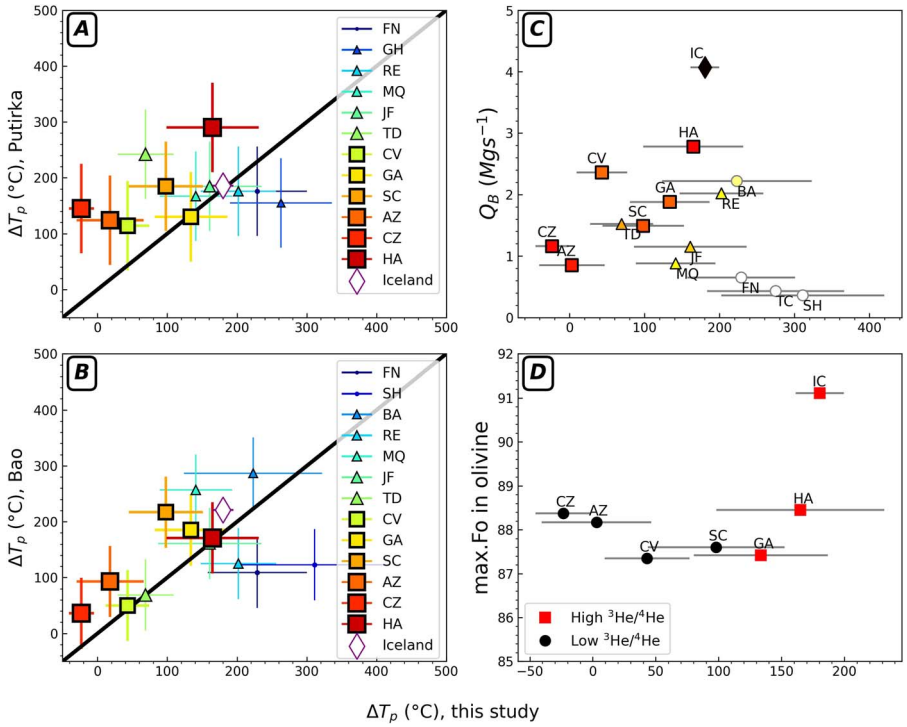

Fig. 10. Comparison of excess temperature (ΔT_p) calculated in this study with those reported in the literature using (*a*) olivine–liquid thermometry by Putirka (2008a) and (*b*) seismic tomography inversion by Bao *et al.* (2022), and our results plotted versus (*c*) volumetric-based plume buoyancy fluxes calculated by Hoggard *et al.* (2020). The ocean islands providing different maximum olivine Fo contents are marked in different symbols (squares: Fo > 87; triangles: Fo85–87; dots: Fo < 85). For ocean islands with Fo > 87 that provide more reliable (ΔT_p) estimates in this study (panel *d*), those with higher $^3He/^4He$ ratios (referring to Jackson *et al.*, 2017, 2020) show generally higher (ΔT_p) than those having low $^3He/^4He$.

with our discussion above, suggesting that the T_{crys}^{prim} calculated using an olivine-only LLD and a low olivine Fo (as the starting point) may be overestimated. Given this and the generally good match between the estimation of ΔT_p in this study and Bao *et al.* (2022), we suggest using olivine with Fo ≥ 85 as a general requirement for acquiring reliable estimates of mantle plume temperature. Overall, 14 ocean islands investigated in this study meet this requirement and were considered in the evaluation of relatively hot or cold hotspots as discussed below.

Bao *et al.* (2022) used the relationship between ΔT_p of hotspots and the multiple of 1σ (45°C) of T_p^{MOR} (calculated using seismic tomography inversion), to classify global hotspots as 'hot' ($\Delta T_p > 3\sigma$), 'warm' ($2\sigma < \Delta T_p < 3\sigma$) and 'cold' ($\Delta T_p < 2\sigma$). Following this approach and taking the error on the T_p of Siqueiros calculated in this study as 1σ (i.e. 12°C), we find that while two ocean islands in this study (Crozet and Azores, ΔT_p of −23°C and 18°C, respectively) are in the category of 'cold' hotspots, the rest are all 'hot'. These generally match with findings of Bao *et al.* (2022), except for Cape Verde and Trindade (ΔT_p of 43 and 69°C, respectively) which were considered as less hot (i.e. 'warm') by Bao *et al.* (2022). This may be explained by two reasons: (1) a single and compositionally identical lithology was considered in the model of Bao *et al.* (2022), whereas many previous studies and our work suggest source lithology variability in the mantle, and (2) different values of 1σ (for T_p^{MOR}) were used in the classification schemes, where that used in this study (only considering the error in T_p of one mid-ocean ridge) is smaller and likely represents the minimum.

Despite these differences, the hotspots found by previous studies to be overlying large ultra-low velocity zones at the core–mantle boundary and having high $^3He/^4He$ ratios (Jackson *et al.*, 2017, 2020) and plume buoyancy fluxes (Hoggard *et al.*, 2020), e.g. Iceland, Hawai'i and Galápagos, are all in the 'hot' hotspots cluster in this study (Fig. 10 c-d), showing an average ΔT_p of ~160°C. Moreover, among the five 'cold' hotspots classified by Bao *et al.* (2022), Crozet (Possession) is the only one investigated in this study which appears as the coldest hotspot (ΔT_p= −23°C) and was found to have a low buoyancy flux and low $^3He/^4He$ ratio (Fig. 10 c-d), implying a passive upwelling at this location. In addition, the ΔT_p we calculated for hotspots providing high-Fo and low-Fo olivines show different degrees of correlation with plume buoyancy fluxes (Fig. 10 c): those in the high-Fo group (Fo_{max}^{obs} >87) show a strong positive correlation, whereas those in the low-Fo group (Fo_{max}^{obs} <85) fall off the trend with values of ΔT_p higher than expected. The latter may be caused by some degrees of overestimation of T_{crys}^{prim}, due to the LLD inversion with low-Fo olivine and/or primitive olivine Fo < 91 at these localities. More accurate estimation of plume temperatures will have to reply on olivines of high Fo contents. This was achieved for eight islands in this study where the analysed olivines are more forsteritic than previously reported; five of them had no olivine data before this study (Supplementary Fig. S2).

CONCLUSION

We reported new petrological estimates of olivine crystallisation temperatures, primary magma temperatures, and mantle potential temperatures and source lithology fractions for multiple ocean islands and the Siqueiros fracture zone (mid-ocean ridge). With a careful screening of the acquired olivine data using a fractionation-diffusion model established in this study, we find that most olivine crystals may have experienced diffusive resetting, thus we took the average crystallisation temperatures (T_{crys}) of the most forsteritic population of olivine from individual ocean islands to derive the primary magma temperature. We attempted

to calculate Fo_{prim} for individual islands based on model results of THERMOCALC but obtained rather high Fo_{prim} (=92–95) that produce abnormally high T_p (up to 1891°C, with a median of 1643°C). Therefore, we took a fixed Fo_{prim}=91 in our calculation and obtained sensible estimates of T_p in good match with values by previous studies, despite the possible variation in Fo_{prim} between localities that needs to be determined in the future.

The calculated T_{crys} values between 1165°C (Crozet) and 1283°C (Hawai'i) yield T_{crys}^{prim} of 1269°C to 1490°C, and T_p between 1327 (±20) °C (Crozet) and 1661 (±108) °C (St. Helena). Using a mid ocean ridge T_p of 1350 (±12) °C calculated using data previously reported for Siqueiros, we obtain excess temperatures of positive values for all localities (ΔT_p=18 ± 49 to 311 ± 109°C) but Crozet (ΔT_p= − 23 ± 22°C). The excess temperatures derived from our calculations are comparable with most results reported by seismic tomography studies, especially for the high-Fo group of ocean islands where olivines of relatively high Fo (≥85) were sampled. The poorer match for localities having less forsteritic olivine between this study and previous work could be due to an overestimation of T_{crys}^{prim} (hence T_p), caused by an olivine-only LLD assumed in this study and/or oversimplification of the mantle source as comprising a single lithology by previous studies. In addition, we observed a strong correlation between the excess temperatures constrained from this study and the plume buoyancy fluxes previously reported for localities where olivine with a Fo > 87 is available. This provides an important reference to future studies on the estimation of plume temperatures using olivine. Moreover, we suggest that when applying a multi-lithological melting model such as that used in this study, the trade-off observed between T_p and source lithology fractions indicates the significance of acquiring additional constraints on the latter (e.g. source pyroxenite fraction), to determine mantle potential temperatures more accurately. The petrological approaches used in this study, including the models developed for investigating diffusive resetting on olivine compositions, can be applied to other localities where mantle upwelling occurs, to advance our understanding of the mantle circulation and dynamics in the Earth's interior.

ACKNOWLEDGEMENTS

We acknowledge Ben Winpenny for sample preparations and Iris Buisman for support in electron microprobe analyses at the University of Cambridge. We thank Mark Hoggard (ANU) for discussions on the plume buoyancy fluxes. Editor Adam Kent and reviewers Claude Herzberg and Eric Brown are greatly acknowledged for providing constructive comments on the manuscript.

SUPPLEMENTARY DATA

Supplementary data are available at *Journal of Petrology* online.

DATA AVAILABILITY

The geochemical data from this study are available at Journal of Petrology online and deposited in EarthChem Library (https://doi.org/10.60520/IEDA/113383). The python codes used for the calculations of olivine crystallisation temperatures along liquid lines of descent and of mantle potential temperatures using variable primitive olivine forsterite contents are available via https://github.com/alexweiranli/OIBolivine and archived in a Zenodo repository (Li, 2025).

FUNDING

This study was funded by Natural Environment Research Council NERC grant NE/T012455/1. W-R. Li acknowledges the support from NERC grant NE/T012455/1, Research Grants Council (RGC) of Hong Kong ECS fund 27302423, and The University of Hong Kong start-up fund. O. Shorttle acknowledges funding from NERC grant NE/T012455/1.

REFERENCES

An, M., Wiens, D. A., Zhao, Y., Feng, M., Nyblade, A., Kanao, M., Li, Y., Maggi, A. & Lévêque, J.-J. (2015). Temperature, lithosphere-asthenosphere boundary, and heat flux beneath the antarctic plate inferred from seismic velocities. *Journal of Geophysical Research: Solid Earth* **120**, 8720–8742. https://doi.org/10.1002/2015JB011917.

Asimow, P. D. & Langmuir, C. H. (2003). The importance of water to oceanic mantle melting regimes. *Nature* **421**, 815–820. https://doi.org/10.1038/nature01429.

Bao, X., Lithgow-Bertelloni, C. R., Jackson, M. G. & Romanowicz, B. (2022). On the relative temperatures of earth's volcanic hotspots and mid-ocean ridges. *Science* **375**, 57–61. https://doi.org/10.1126/science.abj8944.

Batanova, V. G., Thompson, J. M., Danyushevsky, L. V., Portnyagin, M. V., Garbe-Schönberg, D., Hauri, E., Kimura, J.-I., Chang, Q., Senda, R., Goemann, K., Chauvel, C., Campillo, S., Ionov, D. A. & Sobolev, A. V. (2019). New olivine reference material for in situ microanalysis. *Geostandards and Geoanalytical Research* **43**, 453–473. https://doi.org/10.1111/ggr.12266.

Blundy, J., Melekhova, E., Ziberna, L., Humphreys, M. C., Cerantola, V., Brooker, R. A., McCammon, C. A., Pichavant, M. & Ulmer, P. (2020). Effect of redox on Fe–Mg–Mn exchange between olivine and melt and an oxybarometer for basalts. *Contributions to Mineralogy and Petrology* **175**, 103. https://doi.org/10.1007/s00410-020-01736-7.

Chakraborty, S. (2010). Diffusion coefficients in olivine, wadsleyite and ringwoodite. *Reviews in Mineralogy and Geochemistry* **72**, 603–639. https://doi.org/10.2138/rmg.2010.72.13.

Chen, Y. & Zhang, Y. (2008). Olivine dissolution in basaltic melt. *Geochimica et Cosmochimica Acta* **72**, 4756–4777. https://doi.org/10.1016/j.gca.2008.07.014.

Cheng, Z., Zhang, Z., Wang, Z., Wang, F., Mao, Q., Xu, L., Ke, S., Yu, H. & Santosh, M. (2020). Petrogenesis of transitional large igneous province: insights from bimodal volcanic suite in the Tarim large igneous province. *Journal of Geophysical Research: Solid Earth* **125**, e2019JB018382. https://doi.org/10.1029/2019JB018382.

Coogan, L., Saunders, A. & Wilson, R. (2014). Aluminum-in-olivine thermometry of primitive basalts: evidence of an anomalously hot mantle source for large igneous provinces. *Chemical Geology* **368**, 1–10. https://doi.org/10.1016/j.chemgeo.2014.01.004.

Costa, F. (2021). Clocks in magmatic rocks. *Annual Review of Earth and Planetary Sciences* **49**, 231–252. https://doi.org/10.1146/annurev-earth-080320-060708.

Danyushevsky, L. V. & Plechov, P. (2011). Petrolog3: integrated software for modeling crystallization processes. *Geochemistry, Geophysics, Geosystems* **12**. https://doi.org/10.1029/2011GC003516.

Dasgupta, R., Jackson, M. G. & Lee, C.-T. A. (2010). Major element chemistry of ocean island basalts - conditions of mantle melting and heterogeneity of mantle source. *Earth and Planetary Science Letters* **289**, 377–392. https://doi.org/10.1016/j.epsl.2009.11.027.

Davis, F. A., Tangeman, J. A., Tenner, T. J. & Hirschmann, M. M. (2009). The composition of klb-1 peridotite. *American Mineralogist* **94**, 176–180. https://doi.org/10.2138/am.2009.2984.

Droop, G. (1987). A general equation for estimating Fe^{3+} concentrations in ferromagnesian silicates and oxides from microprobe analyses, using stoichiometric criteria. *Mineralogical Magazine* **51**, 431–435. https://doi.org/10.1180/minmag.1987.051.361.10.

Fontaine, F. R., Barruol, G., Tkalčić, H., Wölbern, I., Rümpker, G., Bodin, T. & Haugmard, M. (2015). Crustal and uppermost mantle structure variation beneath la Réunion hotspot track. *Geophysical Journal International* **203**, 107–126. https://doi.org/10.1093/gji/ggv279.

Ghiorso, M. S. (1997). Thermodynamic models of igneous processes. *Annual Review of Earth and Planetary Sciences* **25**, 221–241. https://doi.org/10.1146/annurev.earth.25.1.221.

Gibson, S. & Geist, D. (2010). Geochemical and geophysical estimates of lithospheric thickness variation beneath Galápagos. *Earth and Planetary Science Letters* **300**, 275–286. https://doi.org/10.1016/j.epsl.2010.10.002.

Gleeson, M. L. & Gibson, S. A. (2019). Crustal controls on apparent mantle pyroxenite signals in ocean-island basalts. *Geology* **47**, 321–324. https://doi.org/10.1130/G45759.1.

Green, D. & Ringwood, A. E. (1967). The stability fields of aluminous pyroxene peridotite and garnet peridotite and their relevance in upper mantle structure. *Earth and Planetary Science Letters* **3**, 151–160. https://doi.org/10.1016/0012-821X(67)90027-1.

Green, D., Falloon, T. J., Eggins, S. M. & Yaxley, G. M. (2001). Primary magmas and mantle temperatures. *European Journal of Mineralogy* **13**, 437–451. https://doi.org/10.1127/0935-1221/2001/0013-0437.

Heinonen, J. S., Jennings, E. S. & Riley, T. R. (2015). Crystallisation temperatures of the most mg-rich magmas of the karoo lip on the basis of Al-in-olivine thermometry. *Chemical Geology* **411**, 26–35. https://doi.org/10.1016/j.chemgeo.2015.06.015.

Herzberg, C. & Asimow, P. D. (2008). Petrology of some oceanic island basalts: PRIMELT2. XLS software for primary magma calculation. *Geochemistry, Geophysics, Geosystems* **9**(9). https://doi.org/10.1029/2008GC002057.

Herzberg, C. & Asimow, P. D. (2015). PRIMELT 3 MEGA. XLSM software for primary magma calculation: peridotite primary magma MgO contents from the liquidus to the solidus. *Geochemistry, Geophysics, Geosystems* **16**(2), 563–578. https://doi.org/10.1002/2014GC005631.

Herzberg, C. & O'hara, M. (2002). Plume-associated ultramafic magmas of phanerozoic age. *Journal of Petrology* **43**, 1857–1883. https://doi.org/10.1093/petrology/43.10.1857.

Herzberg, C. T., Asimow, P. D. & Hernández-Montenegro, J. D. (2023). The meaning of pressure for primary magmas: new insights from PRIMELT3-P. *Geochemistry, Geophysics, Geosystems* **24**(1), e2022GC010657. https://doi.org/10.1029/2022GC010657.

Hoggard, M. J., Parnell-Turner, R. & White, N. (2020). Hotspots and mantle plumes revisited: towards reconciling the mantle heat transfer discrepancy. *Earth and Planetary Science Letters* **542**, 116317. https://doi.org/10.1016/j.epsl.2020.116317.

Humphreys, E. R. & Niu, Y. (2009). On the composition of ocean island basalts (oib): the effects of lithospheric thickness variation and mantle metasomatism. *Lithos* **112**, 118–136. https://doi.org/10.1016/j.lithos.2009.04.038.

Ito, M. & Ganguly, J. (2006). Diffusion kinetics of Cr in olivine and 53Mn-53Cr thermochronology of early solar system objects. *Geochimica et Cosmochimica Acta* **70**, 799–809. https://doi.org/10.1016/j.gca.2005.09.020.

Ito, G. & Mahoney, J. J. (2005a). Flow and melting of a heterogeneous mantle: 1. Method and importance to the geochemistry of ocean island and mid-ocean ridge basalts. *Earth and Planetary Science Letters* **230**(1–2), 29–46. https://doi.org/10.1016/j.epsl.2004.10.035.

Ito, G. & Mahoney, J. J. (2005b). Flow and melting of a heterogeneous mantle: 2. Implications for a chemically nonlayered mantle. *Earth and Planetary Science Letters* **230**(1–2), 47–63. https://doi.org/10.1016/j.epsl.2004.10.034.

Jackson, M. G., Konter, J. & Becker, T. (2017). Primordial helium entrained by the hottest mantle plumes. *Nature* **542**, 340–343. https://doi.org/10.1038/nature21023.

Jackson, M. G., Blichert-Toft, J., Halldórsson, S. A., Mundl-Petermeier, A., Bizimis, M., Kurz, M. D., Price, A. A., Harardóttir, S., Willhite, L. N., Breddam, K. *et al.* (2020). Ancient helium and tungsten isotopic signatures preserved in mantle domains least modified by crustal recycling. *Proceedings of the National Academy of Sciences of the United States of America* **117**, 30993–31001. https://doi.org/10.1073/pnas.2009663117.

Jennings, E. S., Holland, T. J., Shorttle, O., Maclennan, J. & Gibson, S. A. (2016). The composition of melts from a heterogeneous mantle and the origin of ferropicrite: application of a thermodynamic model. *Journal of Petrology* **57**, 2289–2310. https://doi.org/10.1093/petrology/egw065.

Jennings, E. S., Gibson, S. A. & Maclennan, J. (2019). Hot primary melts and mantle source for the Paraná-Etendeka flood basalt province: new constraints from Al-in-olivine thermometry. *Chemical Geology* **529**, 119287. https://doi.org/10.1016/j.chemgeo.2019.119287.

Jollands, M., O'Neill, H. S. C., Van Orman, J., Berry, A., Hermann, J., Newville, M. & Lanzirotti, A. (2018). Substitution and diffusion of Cr2+ and Cr3+ in synthetic forsterite and natural olivine at 1200–1500°C and 1 bar. *Geochimica et Cosmochimica Acta* **220**, 407–428. https://doi.org/10.1016/j.gca.2017.09.030.

Kawabata, H., Hanyu, T., Chang, Q., Kimura, J.-I., Nichols, A. R. & Tatsumi, Y. (2011). The petrology and geochemistry of St. Helena alkali basalts: evaluation of the oceanic crust-recycling model for HIMU OIB. *Journal of Petrology* **52**, 791–838. https://doi.org/10.1093/petrology/egr003.

Kelemen, P. B., Dick, H. J. & Quick, J. E. (1992). Formation of harzburgite by pervasive melt/rock reaction in the upper mantle. *Nature* **358**, 635–641. https://doi.org/10.1038/358635a0.

Kogiso, T., Hirschmann, M. & Pertermann, M. (2004). High-pressure partial melting of mafic lithologies in the mantle. *Journal of Petrology* **45**, 2407–2422. https://doi.org/10.1093/petrology/egh057.

Lambart, S., Baker, M. B. & Stolper, E. M. (2016). The role of pyroxenite in basalt genesis: melt-px, a melting parameterization for mantle pyroxenites between 0.9 and 5 gpa. *Journal of Geophysical Research: Solid Earth* **121**, 5708–5735. https://doi.org/10.1002/2015JB012762.

Li, W. (2025). Alexweiranli/OIBolivine: calculations of olivine crystallisation temperatures along basaltic liquid lines of descent and of variable primitiveMatthews, olivine forsterite contents. *Journal of Petrology* (v1.0). Zenodo. https://doi.org/10.5281/zenodo.14744522.

Lynn, K. J., Shea, T. & Garcia, M. O. (2017). Nickel variability in Hawaiian olivine: evaluating the relative contributions from mantle and crustal processes. *American Mineralogist* **102**, 507–518. https://doi.org/10.2138/am-2017-5763.

Maclennan, J. (2008). Concurrent mixing and cooling of melts under Iceland. *Journal of Petrology* **49**(11), 1931–1953. https://doi.org/10.1093/petrology/egn052.

Maclennan, J. (2019). Mafic tiers and transient mushes: evidence from Iceland. *Philosophical Transactions of the Royal Society A* **377**, 20180021. https://doi.org/10.1098/rsta.2018.0021.

Maclennan, J., McKenzie, D., Hilton, F., Gronvöld, K. & Shimizu, N. (2003). Geochemical variability in a single flow from northern Iceland. *Journal of Geophysical Research: Solid Earth* **108**(B1), ECV-4. https://doi.org/10.1029/2000JB000142.

Matthews, S., Shorttle, O. & Maclennan, J. (2016). The temperature of the Icelandic mantle from olivine–spinel aluminum exchange thermometry. *Geochemistry, Geophysics, Geosystems* **17**, 4725–4752. https://doi.org/10.1002/2016GC006497.

Matthews, S., Wong, K., Shorttle, O., Edmonds, M. & Maclennan, J. (2021). Do olivine crystallization temperatures faithfully record mantle temperature variability? *Geochemistry, Geophysics, Geosystems* **22**, e2020GC009157. https://doi.org/10.1029/2020GC009157.

Matthews, S., Wong, K. & Gleeson, M. (2022). pyMelt: An extensible python engine for mantle melting calculations. *Volcanica* **5**(2), 469–475. https://doi.org/10.30909/vol.05.02.469475.

Matzen, A. K., Baker, M. B., Beckett, J. R., & Stolper, E. M. (2011). Fe–Mg Partitioning between Olivine and High-magnesian Melts and the Nature of Hawaiian Parental Liquids. *Journal of Petrology* **52**, 1243–1263. https://doi.org/10.1093/petrology/egq089

Matzen, A. K., Baker, M. B., Beckett, J. R., Wood, B. J. & Stolper, E. M. (2017). The effect of liquid composition on the partitioning of ni between olivine and silicate melt. *Contributions to Mineralogy and Petrology* **172**, 1–18. https://doi.org/10.1007/s00410-016-1319-8.

Morgan, W. J. (1971). Convection plumes in the lower mantle. *Nature* **230**, 42–43. https://doi.org/10.1038/230042a0.

Mutch, E., Maclennan, J., Holland, T. & Buisman, I. (2019). Millennial storage of near-moho magma. *Science* **365**, 260–264. https://doi.org/10.1126/science.aax4092.

Nakagawa, T., Tackley, P. J., Deschamps, F. & Connolly, J. A. (2010). The influence of morb and harzburgite composition on thermo-chemical mantle convection in a 3-d spherical shell with self-consistently calculated mineral physics. *Earth and Planetary Science Letters* **296**, 403–412. https://doi.org/10.1016/j.epsl.2010.05.026.

Phipps Morgan, J. (2001). Thermodynamics of pressure release melting of a veined plum pudding mantle. *Geochemistry, Geophysics, Geosystems* **2**. https://doi.org/10.1029/2000GC000049.

Powell, R., Holland, T. & Worley, B. (1998). Calculating phase diagrams involving solid solutions via non-linear equations, with examples using THERMOCALC. *Journal of Metamorphic Geology* **16**, 577–588. https://doi.org/10.1111/j.1525-1314.1998.00157.x.

Pu, X., Lange, R. A. & Moore, G. (2017). A comparison of olivine–melt thermometers based on D Mg and D Ni: the effects of melt composition, temperature, and pressure with applications to MORBs and hydrous arc basalts. *American Mineralogist* **102**(4), 750–765. https://doi.org/10.2138/am-2017-5879.

Putirka, K. D. (2008a). Excess temperatures at ocean islands: implications for mantle layering and convection. *Geology* **36**, 283–286. https://doi.org/10.1130/G24615A.1.

Putirka, K. D. (2008b). Thermometers and barometers for volcanic systems. *Reviews in Mineralogy and Geochemistry* **69**, 61–120. https://doi.org/10.2138/rmg.2008.69.3.

Putirka, K. D., Perfit, M., Ryerson, F. & Jackson, M. G. (2007). Ambient and excess mantle temperatures, olivine thermometry, and active vs. passive upwelling. *Chemical Geology* **241**, 177–206. https://doi.org/10.1016/j.chemgeo.2007.01.014.

Putirka, K. (2016). Rates and styles of planetary cooling on Earth, Moon, Mars, and Vesta, using new models for oxygen fugacity, ferric-ferrous ratios, olivine-liquid Fe-Mg exchange, and mantle potential temperature. *American Mineralogist*, **101**, 819–840. https://doi.org/10.2138/am-2016-5402.

Ringwood, A. (1962). A model for the upper mantle. *Journal of Geophysical Research* **67**, 857–867. https://doi.org/10.1029/JZ067i002p00857.

Roeder, P. & Emslie, R. (1970). Olivine-liquid equilibrium. *Contributions to Mineralogy and Petrology* **29**, 275–289. https://doi.org/10.1007/BF00371276.

Sack, R. O. & Ghiorso, M. S. (1991a). Chromian spinels as petrogenetic indicators: thermodynamics and petrological applications. *American Mineralogist* **76**, 827–847.

Sack, R. O. & Ghiorso, M. S. (1991b). An internally consistent model for the thermodynamic properties of Fe–Mg-titanomagnetite-aluminate spinels. *Contributions to Mineralogy and Petrology* **106**, 474–505. https://doi.org/10.1007/BF00321989.

Salaün, A., Villemant, B., Semet, M. & Staudacher, T. (2010). Cannibalism of olivinerich cumulate xenoliths during the 1998 eruption of piton de la fournaise (la Réunion hotspot): implications for the generation of magma diversity. *Journal of Volcanology and Geothermal Research* **198**, 187–204. https://doi.org/10.1016/j.jvolgeores.2010.08.022.

Shorttle, O., & Maclennan, J. (2011). Compositional trends of Icelandic basalts: Implications for short-length scale lithological heterogeneity in mantle plumes: COMPOSITIONAL TREND OF ICELANDIC BASALTS. *Geochemistry, Geophysics, Geosystems* **12**. https://doi.org/10.1029/2011gc003748.

Shorttle, O., Maclennan, J. & Lambart, S. (2014). Quantifying lithological variability in the mantle. *Earth and Planetary Science Letters* **395**, 24–40. https://doi.org/10.1016/j.epsl.2014.03.040.

Sobolev, A. V., Hofmann, A. W., Sobolev, S. V. & Nikogosian, I. K. (2005). An olivine-free mantle source of Hawaiian shield basalts. *Nature* **434**, 590–597. https://doi.org/10.1038/nature03411.

Sobolev, A. V., Hofmann, A. W., Kuzmin, D. V., Yaxley, G. M., Arndt, N. T., Chung, S.-L., Danyushevsky, L. V., Elliott, T., Frey, F. A., Garcia, M. O., Gurenko, A. A., Kamenetsky, V. S., Kerr, A. C., Krivolutskaya, N. A., Matvienkov, V. V., Nikogosian, I. K., Rocholl, A., Sigurdsson, I. A., Sushchevskaya, N. M. & Teklay, M. (2007). The amount of recycled crust in sources of mantle-derived melts. *Science* **316**, 412–417. https://doi.org/10.1126/science.1138113.

Spandler, C. & O'Neill, H. S. C. (2010). Diffusion and partition coefficients of minor and trace elements in San Carlos olivine at **1, 300c** with some geochemical implications. *Contributions to Mineralogy and Petrology* **159**, 791–818. https://doi.org/10.1007/s00410-009-0456-8.

Spice, H. E., Fitton, J. G. & Kirstein, L. A. (2016). Temperature fluctuation of the Iceland mantle plume through time. *Geochemistry, Geophysics, Geosystems* **17**, 243–254. https://doi.org/10.1002/2015GC006059.

Stolper, E. M., Shorttle, O., Antoshechkina, P. M. & Asimow, P. D. (2020). The effects of solid–solid phase equilibria on the oxygen fugacity of the upper mantle. *American Mineralogist: Journal of Earth and Planetary Materials* **105**, 1445–1471. https://doi.org/10.2138/am-2020-7162.

Stracke, A., Bizimis, M. & Salters, V. J. (2003). Recycling oceanic crust: quantitative constraints. *Geochemistry, Geophysics, Geosystems* **4**(3). https://doi.org/10.1029/2001GC000223.

Stracke, A., Genske, F., Berndt, J. & Koornneef, J. M. (2019). Ubiquitous ultra-depleted domains in earth's mantle. *Nature Geoscience* **12**, 851–855. https://doi.org/10.1038/s41561-019-0446-z.

Thomson, A. & Maclennan, J. (2013). The distribution of olivine compositions in Icelandic basalts and picrites. *Journal of Petrology* **54**, 745–768. https://doi.org/10.1093/petrology/egs083.

Toplis, M. (2005). The thermodynamics of iron and magnesium partitioning between olivine and liquid: criteria for assessing and predicting equilibrium in natural and experimental systems. *Contributions to Mineralogy and Petrology* **149**, 22–39. https://doi.org/10.1007/s00410-004-0629-4.

Trela, J., Gazel, E., Sobolev, A. V., Moore, L., Bizimis, M., Jicha, B. & Batanova, V. G. (2017). The hottest lavas of the phanerozoic and the survival of deep archaean reservoirs. *Nature Geoscience* **10**, 451–456. https://doi.org/10.1038/ngeo2954.

Walter, M. J. (1998). Melting of garnet peridotite and the origin of komatiite and depleted lithosphere. *Journal of Petrology* **39**, 29–60. https://doi.org/10.1093/petroj/39.1.29.

Wan, Z., Coogan, L. A. & Canil, D. (2008). Experimental calibration of aluminum partitioning between olivine and spinel as a geothermometer. *American Mineralogist* **93**, 1142–1147. https://doi.org/10.2138/am.2008.2758.

Winpenny, B. & Maclennan, J. (2011). A partial record of mixing of mantle melts preserved in Icelandic phenocrysts. *Journal of Petrology* **52**(9), 1791–1812. https://doi.org/10.1093/petrology/egr031.

Wong, K., Ferguson, D., Matthews, S., Morgan, D., Tadesse, A. Z., Sinetebeb, Y. & Yirgu, G. (2022). Exploring rift geodynamics in Ethiopia through olivine–spinel Al-exchange thermometry and rare-earth element distributions. *Earth and Planetary Science Letters* **597**, 117820. https://doi.org/10.1016/j.epsl.2022.117820.

Wu, Y.-D., Yang, J.-H., Stagno, V., Nekrylov, N., Wang, J.-T. & Wang, H. (2022). Redox heterogeneity of picritic lavas with respect to their mantle sources in the Emeishan large igneous province. *Geochimica et Cosmochimica Acta* **320**, 161–178. https://doi.org/10.1016/j.gca.2022.01.001.

Xu, R. & Liu, Y. (2016). Al-in-olivine thermometry evidence for the mantle plume origin of the Emeishan large igneous province. *Lithos* **266-267**, 362–366. https://doi.org/10.1016/j.lithos.2016.10.016.

Zanon, V. (2015). Chapter 5 the magmatism of the Azores islands. *Geological Society, London, Memoirs* **44**, 51–64. https://doi.org/10.1144/M44.5.

Zhang, L., Ren, Z.-Y., Zhang, L., Wu, Y.-D., Qian, S.-P., Xia, X.-P. & Xu, Y.-G. (2021). Nature of the mantle plume under the Emeishan large igneous province: constraints from olivine–hosted melt inclusions of the Lijiang picrites. *Journal of Geophysical Research: Solid Earth* **126**, e2020JB021022. https://doi.org/10.1029/2020JB021022.

Zhang, Y., Namur, O., Li, W., Shorttle, O., Gazel, E., Jennings, E., Thy, P., Grove, T. L. & Charlier, B. (2023). An extended calibration of the olivine–spinel aluminum exchange thermometer: application to the melting conditions and mantle lithologies of large igneous provinces. *Journal of Petrology* **64**. https://doi.org/10.1093/petrology/egad077.

Journal of Petrology, 2025, **66**, egaf033
https://doi.org/10.1093/petrology/egaf033
Original Manuscript